Resilient Operations in Space with Digital Twin Integration for Solar PV and Energy Storage

Shayan Ebrahimi[1], Mohammad Seyedi[1], SM Safayet Ullah[1], and Farzad Ferdowsi[1,*]

[1]Electrical & Computer Engineering Dept., University of Louisiana at Lafayette, Lafayette, LA, 70503, USA (

[*]Corresponding author: ferdowsi@louisiana.edu

Abstract

Space missions would not be possible without an available, reliable, autonomous, and resilient power system. Space-based power systems are different than Earth's grid in terms of generation sources, needs, structure, and controllability. This research paper introduces a groundbreaking approach employing digital twin technology to emulate and enhance the performance of a physical nanogrid plant representing such a space-based power system. The proposed system encompasses three DC converters, a DC source, and a modular battery storage unit feeding a variable load. Rigorous testing across diverse operating points establishes the digital twin's high-fidelity real-time representation, with root mean square error (RMSE) values consistently below 5%. The principal innovation lies in leveraging this digital twin to fortify system resilience against unforeseen events, beyond the capabilities of existing controllers and autonomy levels. By simulating scenarios that the current system may not be primed for, the digital twin provides operators with the tools to proactively respond to disruptions. Importantly, the approach offers an invaluable tool for scenarios where physical access to components is limited. This research introduces a modular battery storage solution as a key augmentation, capable of seamlessly compensating for power shortages at the source end that might arise from the dust effect on the Lunar surface or unexpected faults in the system. The proposed holistic approach not only validates the fidelity of the digital twin but also underscores its potential to revolutionize system operation, safeguard against uncertainties, and expedite response strategies in the face of unexpected contingencies. The proposed approach also paves the way for future development.

Keywords: Digital Twin, Resilience, Space Power Stations

1. Introduction

The advent of intelligent systems followed by the Fourth Industrial Revolution or Industry 4.0, made digital twin (DT) platforms a feasible alternative to analyze and evaluate the performance of dynamical systems enabling critical decision-making. To be more specific, the emergence of artificial intelligence (AI) techniques, the Internet of Things (IoT), and cyber-physical systems (CPSs) has a significantly vital role to play in this area Bazmohammadi et al., 2022; Ebrahimi, Ullah, Ferdowsi & Barati, 2022.

Although twinning originated in NASA's Apollo program in the 1960s Allen, 2021 and later on appeared in aerospace and aviation sectorsShafto et al., 2012, it quickly found use cases in various fields ranging from manufacturing Qi & Tao, 2018; Yang et al., 2022 to healthcare and remote surgery systems Laaki et al., 2019; Y. Liu et al., 2019. At a larger scale, in Deren et al., 2021, for instance, the authors discuss applications and features of digital twin-based smart cities. To date, numerous DT applications have been deployed in many industries which named DT one of the Top 10 Strategic Technology Trends in 2018 by Gartner Garfinkel, 2018. Furthermore, the DT market is expected to increase from USD 3.8 billion in 2019 to USD 35.8 billion by 2025 due to the rising use of new technologies such as IoT and cloud computing Eirinakis et al., 2020.

According to the report provided by the US Department of Energy DoE, 2003, modern power grids are one of the most complicated engineering systems which makes the North American power grids the pinnacle of twentieth-century engineering achievement. In addition, increased installation of renewable energy systems along with Inverter-Based Resources (IBR) is making power grids substantially complex Ebrahimi, Ullah & Ferdowsi, 2024. This perplexity makes traditional computer simulations unable to provide accurate analysis and evaluation of the systems, especially in situations where model fidelity is important.

To build a virtual representation of a physical system (PS), an advanced high-precision modeling platform is required. Various software and tools can be used to develop a DT model of a PS. In Beguery et al., 2019, a Matlab GUI toolbox is utilized to build an MGDT to address some specific customer requests using a real Energy Management System (EMS) algorithm. In a 2019 study Pileggi et al., 2019, python is used to develop a DT model of a battery system to find and detect anomalies for CPS purposes.

In addition, each DT model can be developed based on two fundamental principles including physics-based or data-driven. A Physics-based DT model is built based on principal standard assumptions of physics and mathematics. A data-driven DT model, however, is based on statistical techniques to derive an architectural arrangement of a case study model from its data. Each DT fundamental principle has its advantages and disadvantages. To name a few, physics-based models are frequently applied when fundamental principles of case studies are digested. Even though they have been applied for many years, they are restricted led by an insufficient understanding of the underlying architecture of case studies caused by mathematical constraints. Data-driven models, nevertheless, seem to be more flexible since they rely on ample data available from case studies. They also suffer from a scarcity of a good understanding of fundamental principles for case studies.

Eventually, both physics-based and data-driven DT model have their own merits and demerits, and they can be selected based on available knowledge of a case study and the application. In Hong & Apolinario, 2022, the digital twin concept is utilized at the system level. Networked microgrids are represented by neural networks where the generated power of different units such as solar, fuel cell, battery, and diesel generators are predicted. Typhoon Hardware-in-the-Loop (HIL) software is used in Ebrahimi, Safayet Ullah & Ferdowsi, 2022 to build a physics-based DT model of an IEEE 4-bus to enhance the PV system performance via mitigating voltage violation and fluctuation.

The beauty of DT models is their ability to mimic the behavior of PS accurately. The PS, however, has a vital role to play in developing the DT model since without the presence of a PS, the DT model is nonsensical. In other words, a DT model should be a virtual replica of an existing system to be claimed as a digital twin. Otherwise, there is no difference between conventional computer simulations where the model is built based on certain assumptions and imaginary actual systems, or IEEE standard systems. In a 2020 study H. Pan et al., 2020, a DT model of a power substation system, Cai-Lun station, is built. Although authors in Yuan & Xie, 2023 present an RL-based DT model to address load commitment issues, there is no actual existing microgrid system represented as the PS. In a 2019 study Béguery et al., 2019, the DiSiPl platform is used to develop a DT model to tackle energy management system issues. It lacks, however, the presence of an actual microgrid to build the DT model based on.

The same research gap, the lack of PS, is also observed in Li, Cui, Cai, Su & Wang, 2023 where authors propose an AI-driven algorithm for digital twinning to address demand response issues for microgrids comprised of renewable sources. In M. Pan et al., 2023, an RL-driven DT model is developed to schedule batteries for optimum energy management. The paper, however, lacks information about sensors, synchronization, and even the specifications of components within the physical plant. Cheng et al., 2023 presents a digital twinning framework for a microgrid where a physical plant exists; however, the communication between the digital model and the plant is not discussed. Additionally, it is not well discussed to what extent the digitalized microgrid mimics the behavioral dynamics of the physical plant.

Another gap found in the digital twinning studies is the lack of model fidelity assessment. In other words, the accuracy of DT models with respect to the PS's behavior has not been well discussed. The fidelity of a DT model can be assessed by applying standard measurement metrics such as Root Mean Square Error (RMSE), Mean Absolute Percentage Error (MAPE), or R-squared error. Ebrahimi, Safayet Ullah et al., 2024. By assessing the output results of the DT and PS via standard measurement metrics, systems operators can ensure the performance of the DT is close enough to the PS. Thus, validation is fundamental for the appraisal of DT models. This has a vital role to play in case studies where the PS is far away from its control center like space applications.

Several studies present DT models with the presence of PS, but they suffer from a lack of fidelity assessment. In Padmawansa et al., 2023, a DT model is developed to predict the required cycle count and stress levels of a battery energy storage system. Neither the DT model is built based on an actual battery system, nor the fidelity of the DT performance is assessed. In another 2023 study Li, Cui, Cai & Su, 2023, AI-driven and a heuristic algorithm are applied to develop a DT model of smart homes connected to renewables. The DT model, however, lacks a fidelity assessment test. In Saad et al., 2020, the implementation of energy cyber-physical systems(ECPSs) utilizing two DT models to cover high-bandwidth and the low bandwidth applications is presented. The DT models, however, are not evaluated with the results of an actual system. In a 2022 study Lopez et al., 2022, a fault identification framework is presented for low-level components of a DT to ensure the dynamic stability of the components. The presented framework consists of a Self Organized Map (SOM) Neural Network to measure the faults within a Real-time model. Like other DT studies, the scarcity of fidelity assessment tests for the DT model is observed in this research work.

Pursuing NASA's universe exploration plans, the Artemis program aims to take humans to the Moon by 2025 and establish a sustainable presence on the lunar surface Artemis, 2022. Unlike terrestrial microgrids (MGs), the design of the non-terrestrial MG system is quite different. Due to the dusty atmosphere of the Moon NASA, 2023, solar panels' deliverable power can substantially be impacted and reduced. Therefore, a backup source, commonly a battery storage system (BSS) is required to support solar PV. The program aims to land the first woman and next man on the Lunar surface by 2025, to establish sustainable exploration and utilization of the Moon by the end of the decade. Also, this program is expected to pave the way for human exploration of Mars and other destinations in the solar system. A space-based resilient power system is critical for almost all aspects of future Lunar exploration endeavors, and the design of such a power system requires extensive research. Cost, safety, and flexibility have been always the three main concerns for research in the power system area. Utilization of a digital twin will accelerate research tasks while maintaining a high level of fidelity.

In this study, DT is utilized to mimic the actual MG system representing a Lunar-type MG, Fig.1. The prototype for this case study is designed and developed by the power systems Control Advancement and Resilience Enhancement (CARE) team at the University of Louisiana at Lafayette. To address the above-mentioned issues in the DT area, the research team leveraged DT as an effective tool that yields significant benefits in augmenting the control of space-based power systems. Once the DT model is developed, the DT will be undergoing fidelity assessment tests in phase I. In these tests, the output voltage of the DT model is logged via measurement devices and compared with the PS.

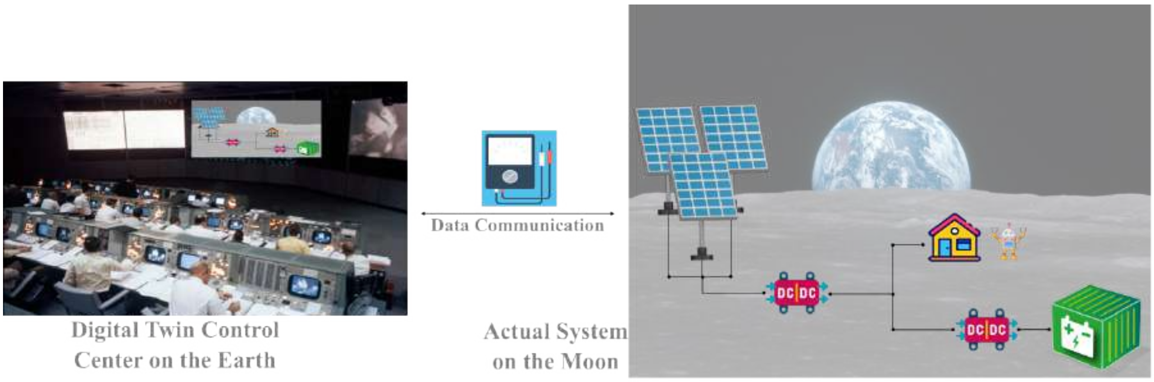

Figure 1: The concept of the MGDT system for Lunar MG systems

Root mean square error (RMSE) is a fundamental measurement unit that is calculated and monitored to be consistently below 5 %. After the DT model is successfully validated, the DT model is utilized to perform certain real-time what-if scenarios instead of the PS. The outcomes of the scenarios can substantially help decision-makers have a better understanding of the performance of the PS in real situations. Thus, operators can provide solid solutions during emergencies or for critical decision-making beyond expected situations. The technical contributions of this research study are summarized below.

- **Development of a High-Fidelity Real-Time Model:** This study pioneers the creation of a high-fidelity, real-time model representing an authentic space-based power system. This model stands as a crucial advancement in accurately simulating such systems.

- **Introduction of Fidelity Assessment for Power System Digital Twins:** Significantly, this research introduces the concept of fidelity assessment for power system digital twins, emphasizing the necessity for standardized evaluation criteria. This marks a pioneering step towards establishing benchmarks in this field.

- **Validation of Real-Time Decision Making using Digital Twins:** The research proposes and validates the concept of real-time decision-making within digital twins for power systems. This breakthrough facilitates critical decision-making, particularly in scenarios where physical access to the system is constrained.

In this paper, System Description and Modeling are explained in section II along with a detailed description of each control mode including their mathematical formulations. Establishing the Digital Twin Model is discussed in section III. In this section, DT development is discussed in subsection A, and PS is described in subsection B. Eventually, section IV covers the results and discussion followed by the conclusion section.

2. System Description and Modeling

The overview of the MGDT system is shown in Fig. 2. As can be seen, the solar PV system plays a key role in space-based power systems. Due to the dusty atmosphere of the Moon, the battery system will discharge to support the solar PV to meet the demand. In normal operation, since the solar PV system is able to supply the load demand, the battery will be charged through the bi-directional DC-DC converter.

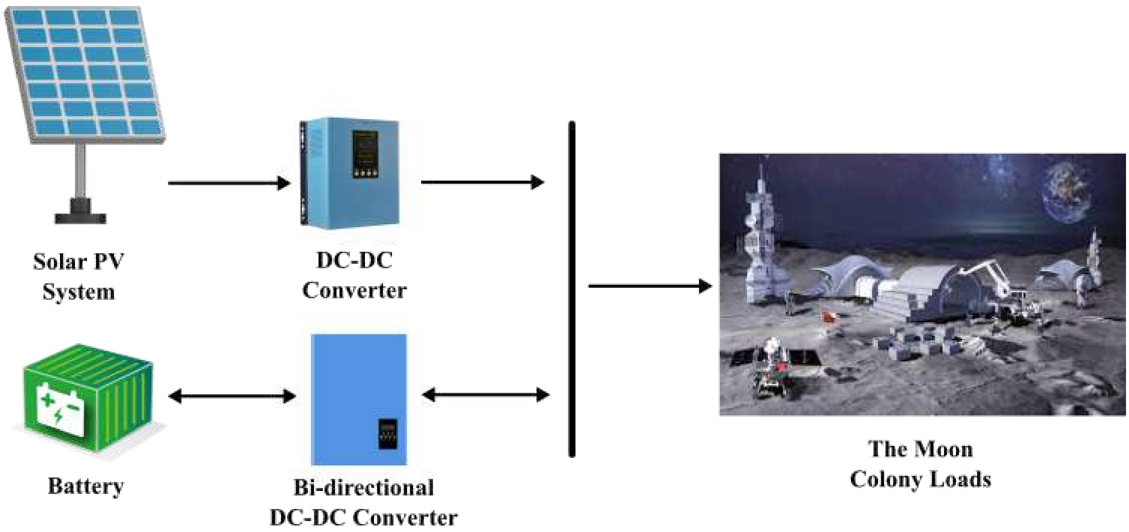

Figure 2: The overview of a Lunar MG system

In this case study, the control unit has a vital role to play in accurate system operation due to supplying load demand. The performance of the control during each mode of operation for the PV system and the battery system is illustrated in Fig. 3.

According to the flowchart, the total amount of the solar PV system's available power is calculated in every sample time after measuring voltages and currents. If the available power from the solar PV can meet the load demand, the controller checks the state of charge (SOC) of the Lithium-ion battery. In case the battery is fully charged, the control system will go to mode 0 representing the normal operation. In this mode the battery system is disconnected from the MG and only the solar PV is responsible for supplying the loads.

If the SOC is below the predefined value (like 80%), the control system will go to mode 1 which is constant current (CC) charging for the battery. When the SOC of the battery reaches 80%, the control system switches to mode 2 and the battery is charged under constant voltage (CV) until it is fully charged. Eventually, mode 3 happens when the solar PV does not have sufficient power to meet the load demand. Thus, the PV system is immediately disconnected from the load bus and the battery is connected to the supply load demand. Each control mode of operation will be explained further in the following sections.

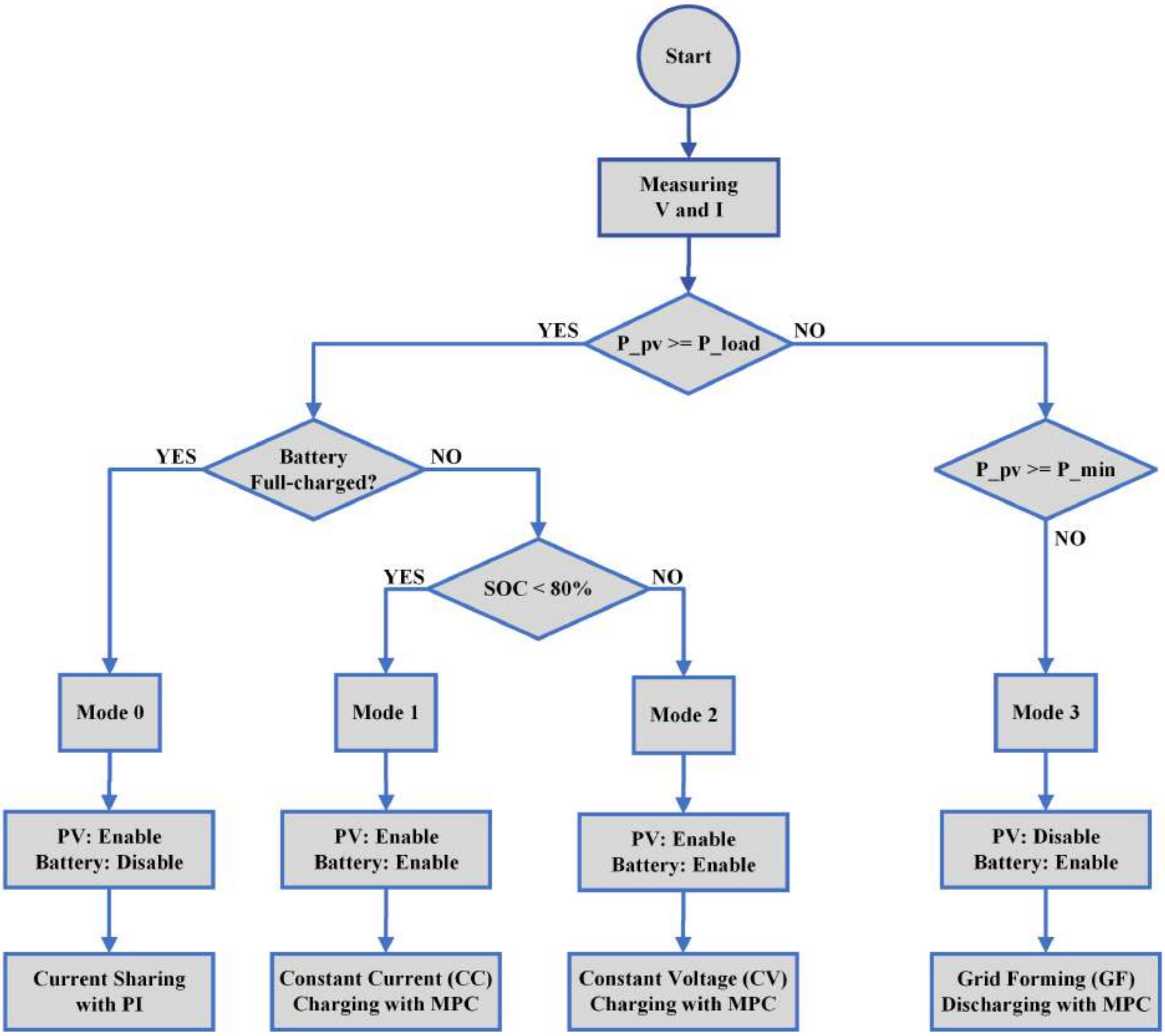

Figure 3: MGDT Flowchart of Control strategy for each Mode

Fig. 4 depicts the Bi-directional buck-boost DC-DC battery converter. In charging modes, the buck side of the converter is activated which includes an inductor, L, with the internal resistor, R_L, and capacitor, C_{bat}. This will happen via S_1 and the antiparallel diode of S_2. For discharging modes, however, the boost side will be activated and connected to C_{dc}. To do so, S_2 will be triggered and the boosted current will be passed through the antiparallel diode of S_1.

To continuously meet the load demand, the battery controller should work closely with the Solar PV system. Thus, the control strategy for the battery is comprised of 5 unique modes to have better collaboration with Solar PV. To implement the control strategy for the battery, Model Predictive Control (MPC) is applied to perform operation modes Rajesh et al., 2019. The inductor current is formulated in (1).

$$L\frac{dI_L(t)}{dt} = V_{bat} - R_L I_L(t) - BV_{dc} \tag{1}$$

Where L and R_L represent the inductance and the inductor's internal resistor. V_{bat} and I_L are the battery voltage and inductor current. B denotes switching states which

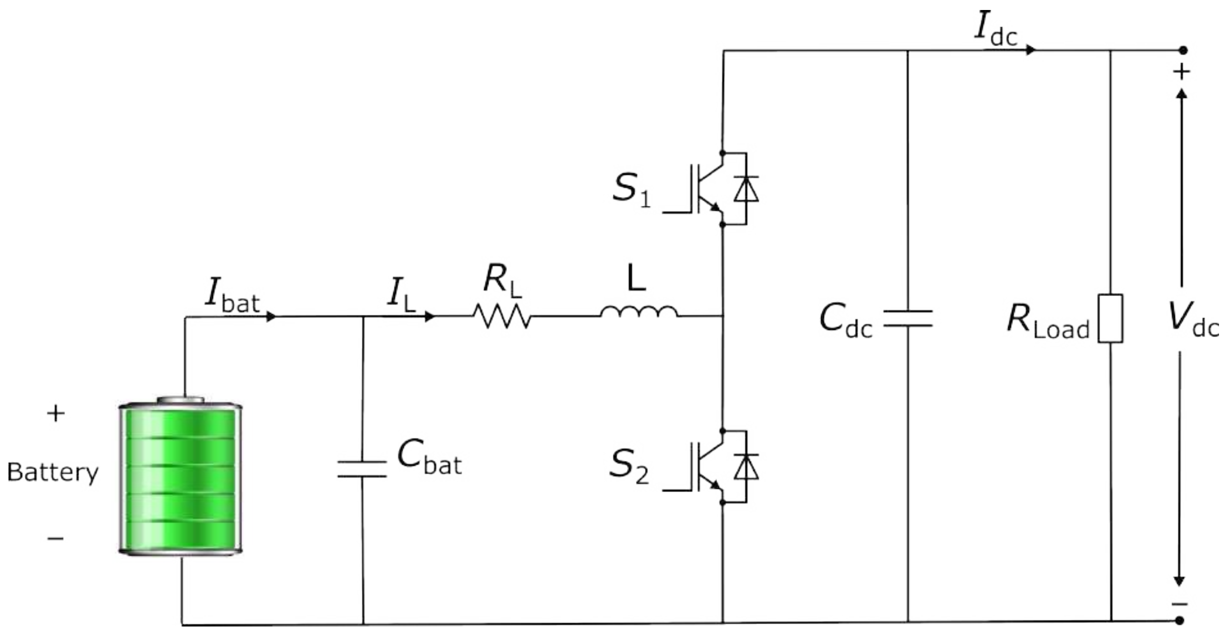

Figure 4: Bi-directional buck-boost

indicates S_1 for charging modes and 1 - S_2 for discharging modes.

On the other hand, the dynamic behavior for the capacitor voltage corresponds to the charging or discharging operational mode. Equations (2) and (3) correspond to the charge and discharge modes respectively.

$$C_{bat}\frac{dV_{bat}(t)}{dt} = I_L(t) - I_{bat} \tag{2}$$

$$C_{dc}\frac{dV_{dc}(t)}{dt} = (1 - S_2)I_L(t) - \frac{V_{dc}(t)}{R_{Load}} \tag{3}$$

Where C_{bat} and C_{dc} are buck side and boost side capacitors, respectively. V_{dc} and I_{bat} are load bus voltage and the current flowing to the battery. R_{Load} is the impedance of load which in this case study is fully resistive.

To analyze the dynamical behavior via MPC, the Euler forward method is applied to approximate the derivatives of the above-mentioned equations for the Bi-directional buck-boost converterRivera et al., 2016.

$$\frac{dX(t)}{dt} \simeq \frac{X(k+1) - X(k)}{T_s} \tag{4}$$

Where T_s is sample time. Each mode's dynamic behavior will be discussed in detail along with their equations in the following sections.

2.1 Mode 0 - Normal Operation

In this mode of operation, solar PV is capable of supplying load demand. Fig. 5 illustrates the block diagram of the current sharing approach applied to control 3 solar PV agents.

This method ensures avoiding circulating currents for the three solar PVs mitigating

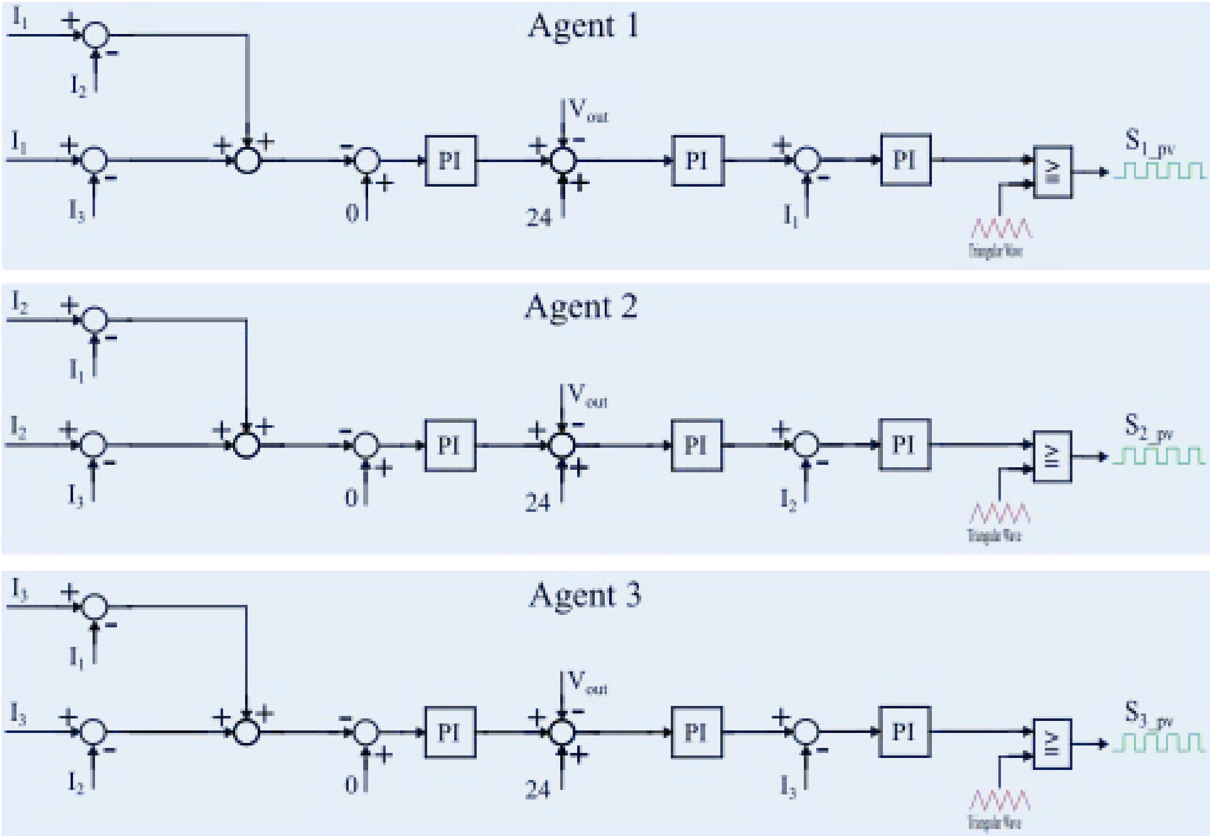

Figure 5: Current Sharing Control Diagram

the negative impacts of circulating currents Ghanbari & Bhattacharya, 2020. Since the PV system is able to fully supply the load (mode 0), the controller puts the battery in idle mode, Fig. 6. This will isolate the battery from the MG.

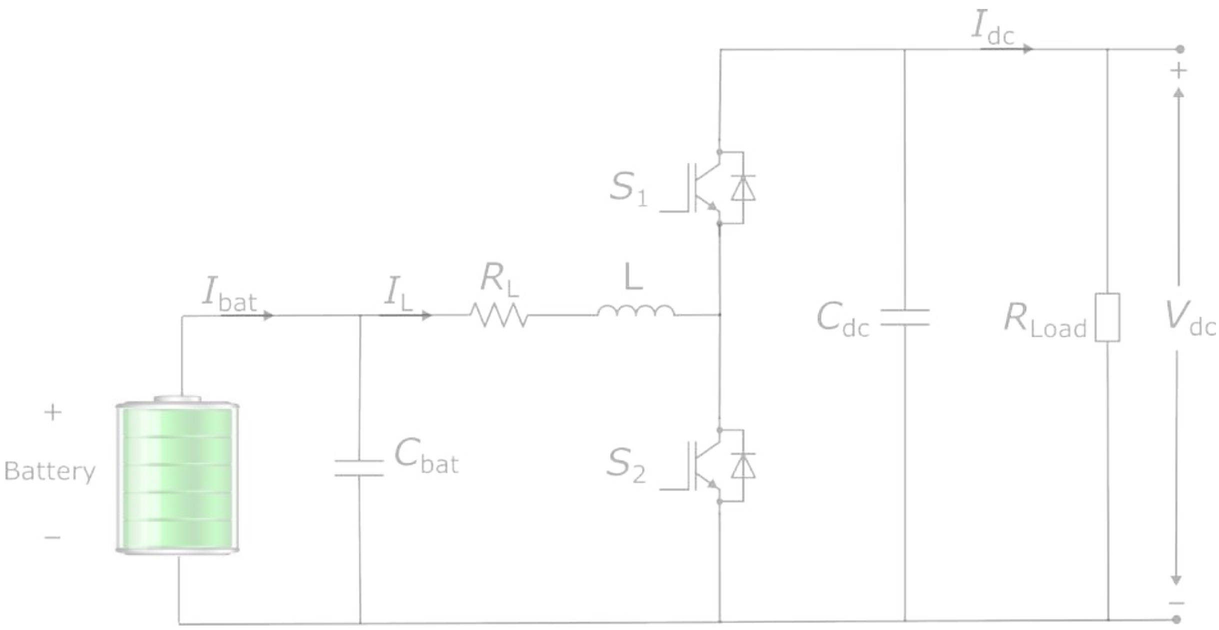

Figure 6: Configuration of Bi-directional buck-boost Under Normal Operation

2.2 Mode 1 - Constant Current (CC) Charging

The battery in this mode is charged with a controlled and limited current flow. CC charging provides some benefits like fast charging, balancing cell voltage, and safety. This method of charging, however, is commonly used for certain types of batteries, such as lithium-ion batteries, to ensure safe and efficient charging Brenna et al., 2020.

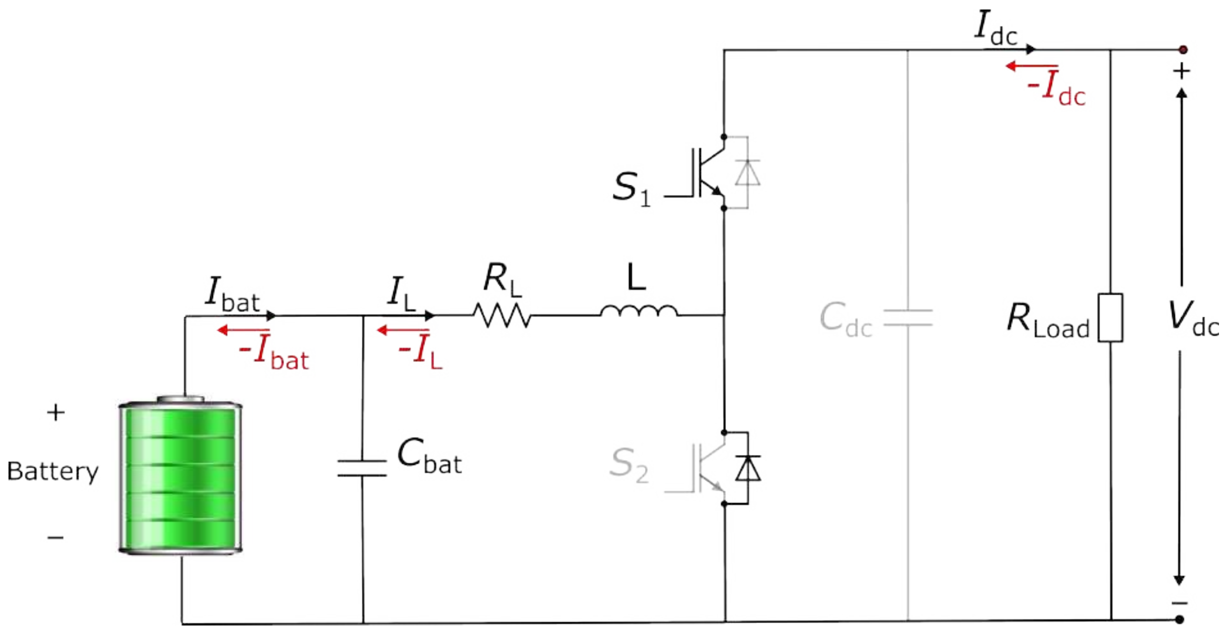

Figure 7: Configuration of Bi-directional buck-boost Under Charging Modes

Fig. 7 shows the configuration of the bi-directional buck-boost for this application. Since the direction of the current flow is reversed due to the charging mode, 1 will be updated as:

$$L\frac{dI_L(t)}{dt} = -V_{bat}(t) - R_L I_L(t) + S_1 V_{dc} \tag{5}$$

Where S_1 can be either 1 or 0 depending on the switching status. To calculate I_L at time $k+1$ with sample time T_s, forward Euler approximation is applied to discretize the derivative of the inductor current. So, by applying 4 to 5, (6) is formed.

$$\begin{aligned} I_L(k+1) = &\frac{S_1(k)T_s}{L} V_{dc}(k) \\ &+ \left(1 - \frac{R_L T_s}{L}\right) I_L(k) - \frac{T_s}{L} V_{\text{bat}}(k) \end{aligned} \tag{6}$$

The goal is to minimize the error between the predicted I_L at the time $k+1$ and the reference current to charge the battery in CC mode. Thus, the cost function is considered as follows:

$$\begin{aligned} G_{cc}(k+1) = &|I_L^*(k) - I_L(k+1)| \\ &+ \lambda_{cc}|S_1(k) - S_1(k-1)| \end{aligned} \tag{7}$$

Where $I_L^*(k)$ is the inductor reference current and λ_{cc} is a weighting factor for CC charging mode. Unless the battery's SOC reaches 80%, the battery remains in the CC mode.

2.3 Mode 2 - Constant Voltage (CV) Charging

To avoid overcharging and ensure desirable performance, durability, and safety of the battery, a resilient integration of charging modes (e.g., CC & CV) is required. Thus, once the SOC of the battery reaches 80%, the battery goes into the CV mode. In this mode, a constant voltage will be held at the battery's terminal until the SOC reaches 100%.

The configuration of the bi-directional buck-boost and direction of the current are the same as in CC mode shown in Fig. 7. For analyzing the dynamics for this mode, the output voltage of the converter and the inductor current are formulated as follows:

$$L\frac{dI_L(t)}{dt} = -V_{bat}(t) - R_L I_L(t) + S_1 V_{dc} \tag{8}$$

$$C_{bat}\frac{dV_{bat}(t)}{dt} = I_L(t) - I_{bat}(t) \tag{9}$$

In the next step, the state space representation of (8) and (9),is formed in (11) using (10):

$$\dot{X}(t) = AX(t) + BU(t, S_1(t)) \tag{10}$$

Thus, the result is:

$$\begin{aligned}\begin{bmatrix} \frac{dI_L(t)}{dt} \\ \frac{dV_{\text{bat}}(t)}{dt} \end{bmatrix} &= \begin{bmatrix} \frac{-R_L}{L} & \frac{-1}{L} \\ \frac{-1}{C_{\text{bat}}} & 0 \end{bmatrix} \begin{bmatrix} I_L(t) \\ V_{\text{bat}}(t) \end{bmatrix} \\ &+ \begin{bmatrix} \frac{-1}{L} & 0 \\ 0 & \frac{-1}{C_{\text{bat}}} \end{bmatrix} \begin{bmatrix} S_1 V_{dc} \\ I_{\text{bat}}(t) \end{bmatrix}\end{aligned} \tag{11}$$

To obtain the predicted value of V_{bat} at time $k+1$ with sample time T_s, the discretization of the state space representation in 10 can be written as follows for a better parameter-varying relevant Toth et al., 2010:

$$X(k+1) = A_d X(k) + B_d U(k, S_1(k)) \tag{12}$$

Where $A_d = e^{AT_s}$ and $B_d = A^{-1}(A_d - 1)B$ in discrete-time arrangement with sample time T_s. Therefore, the discretization of (11) is (13).

$$\begin{bmatrix} I_L(k+1) \\ V_{\text{bat}}(k+1) \end{bmatrix} = e^{\begin{bmatrix} \frac{-R_L}{L} & \frac{-1}{L} \\ \frac{-1}{C_{\text{bat}}} & 0 \end{bmatrix} T_s} \begin{bmatrix} I_L(k) \\ V_{\text{bat}}(k) \end{bmatrix} + \begin{bmatrix} \frac{-R_L}{L} & \frac{-1}{L} \\ \frac{-1}{C_{\text{bat}}} & 0 \end{bmatrix}^{-1} \left(e^{\begin{bmatrix} \frac{-R_L}{L} & \frac{-1}{L} \\ \frac{-1}{C_{\text{bat}}} & 0 \end{bmatrix} T_s} - 1\right) \begin{bmatrix} \frac{-1}{L} & 0 \\ 0 & \frac{-1}{C_{\text{bat}}} \end{bmatrix} \begin{bmatrix} S_1 V_{dc} \\ I_{\text{bat}}(k) \end{bmatrix} \tag{13}$$

To minimize the difference between the predicted value of V_{bat} at time $k+1$ and the reference battery charging voltage for CV, the cost function is formulated as follows:

$$G_{cv}(k+1) = |V_{\text{bat}}^{*}(k) - V_{\text{bat}}(k+1)| \\ + \lambda_{cv}|S_1(k) - S_1(k-1)| \tag{14}$$

Where $V_{bat}^{*}(k)$ is the battery reference charging voltage and λ_{cv} is a weighting factor for CV charging mode. The battery is charged with constant voltage with limited current until the SOC reaches 100%. To limit the charging current in the CV mode, the appropriate reference charging voltage is selected.

2.4 Mode 3 - Grid Forming (GF) Discharging

Since the PV system is unable to maintain the load bus voltage at the desired value and the solar fails to meet the demand, the battery controller disconnects the main grid from the DC load bus and supplies the load in islanding mode. Therefore, the battery discharges to keep the DC load bus at the desired voltage and serve the demand.

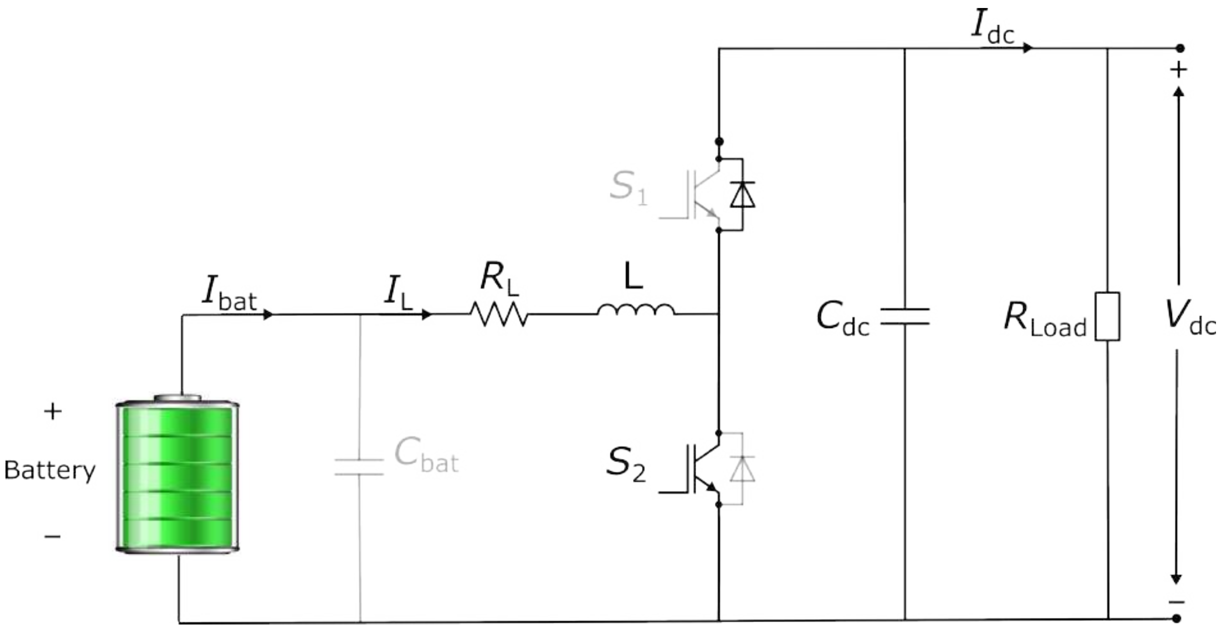

Figure 8: Configuration of Bi-directional buck-boost Converter Under Discharging Modes

The configuration of the bi-directional buck-boost converter in the GF mode is shown in Fig. 8. In this mode, the battery will form and create the grid in the GF mode. Not only does the battery supply the desired voltage for the DC load bus, but it also delivers the amount of current required for the load through the boost side of the bi-directional buck-boost converter. For analyzing the dynamics in the GF mode, the output voltage of the boost side of the bi-directional buck-boost as well as the inductor current are formulated as follows:

$$L\frac{dI_L(t)}{dt} = V_{bat}(t) - R_L I_L(t) - (1 - S_2)V_{dc}(t) \tag{15}$$

$$C_{dc}\frac{dV_{dc}(t)}{dt} = (1 - S_2)I_L(t) - \frac{V_{dc}(t)}{R_{Load}} \tag{16}$$

To better analyze the impact of parameter variations, the state space representation 10 is applied. Thus, the result is:

$$\begin{aligned}\begin{bmatrix}\frac{dI_L(t)}{dt}\\ \frac{dV_{dc}(t)}{dt}\end{bmatrix} = \begin{bmatrix}\frac{-R_L}{L} & \frac{-1}{L}\\ \frac{-1}{C_{dc}} & \frac{-1}{R_{obs}C_{dc}}\end{bmatrix}\begin{bmatrix}(1 - S_2)I_L(t)\\ (1 - S_2)V_{dc}(t)\end{bmatrix}\\ + \begin{bmatrix}\frac{1}{L} & 0\\ 0 & 0\end{bmatrix}\begin{bmatrix}V_{\text{bat}}(t)\\ I_{\text{bat}}(t)\end{bmatrix}\end{aligned} \tag{17}$$

To obtain the predicted value of V_{dc} at time $k + 1$ with sample time T_s, the discretization of the state space representation is formed in 17 using 12 can be formulated as 18.

$$\begin{bmatrix}I_L(k+1)\\ V_{dc}(k+1)\end{bmatrix} = e^{\begin{bmatrix}\frac{-R_L}{L} & \frac{-1}{L}\\ \frac{-1}{C_{dc}} & \frac{-1}{R_{obs}C_{dc}}\end{bmatrix}T_s}\begin{bmatrix}(1 - S_2)I_L(k)\\ (1 - S_2)V_{bat}(k)\end{bmatrix} + \begin{bmatrix}\frac{-R_L}{L} & \frac{-1}{L}\\ \frac{-1}{C_{dc}} & \frac{-1}{R_{obs}C_{dc}}\end{bmatrix}^{-1}(e^{\begin{bmatrix}\frac{-R_L}{L} & \frac{-1}{L}\\ \frac{-1}{C_{dc}} & \frac{-1}{R_{obs}C_{dc}}\end{bmatrix}T_s} - 1)\begin{bmatrix}\frac{1}{L} & 0\\ 0 & 0\end{bmatrix}\begin{bmatrix}V_{bat}(k)\\ I_{bat}(k)\end{bmatrix} \tag{18}$$

One of the goals in this mode is to minimize the error between the predicted I_L at the time k + 1 and a reference current in GF mode. This reference current is indeed the current demanded from the observed load at that time. Thus, this reference current can be calculated as:

$$I_{dem} = \frac{V_{dc}}{R_{obs}} \tag{19}$$

Where I_{dem} is the current demanded by the load and R_{obs} is the amount of observed load in Ω. In this case study, it is assumed that R_{obs} is known through the loads' switching states. The second goal is to minimize the difference between the prediction of future V_{dc} at time k + 1 and the reference DC load bus voltage. Therefore, the cost function is determined as follows:

$$\begin{aligned}G_{gf}(k+1) =& |V^*_{\text{ref, dc}}(k) - V_{\text{dc}}(k+1)|\\ &+ |I^*_{\text{ref, gf}}(k) - I_L(k+1)|\\ &+ \lambda_{gf}|S_2(k) - S_2(k-1)|\end{aligned} \tag{20}$$

Where $V^*_{ref,dc}(k)$ is the dc load bus reference voltage and λ_{gf} is a weighting factor for the GF discharging mode. $I^*_{ref,gf}(k)$ is the battery reference current demanded by the load and can be calculated through Eq. 19. The goal in the GF mode, however, is to keep the DC load bus at the desired voltage, $V^*_{ref,dc}(k)$, in addition to supplying the amount of current required at the load side.

3. Establishing the Digital Twin Model

A DT testbed is designed and developed by the power systems Control Advancement and Resilience Enhancement (CARE) team at the University of Louisiana at Lafayette illustrated in Fig. 9. The testbed is comprised of the physical microgrid plant and a high-fidelity virtual representation developed on the Typhoon HIL simulator. The characteristics of the DT and the actual system are further described in the following sections.

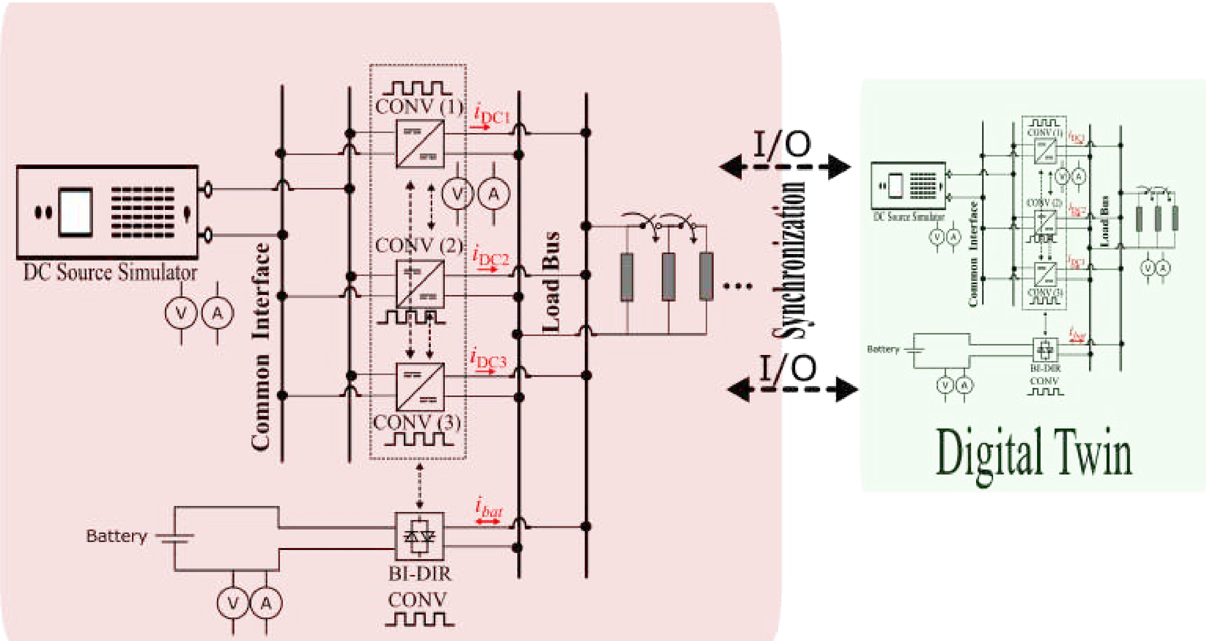

Figure 9: DC microgrid live DT

3.1 Design of MG Digital Twin (DT)

The real-time DT model of the DC microgrid is developed on the Typhoon HIL 402 environment. According to Fig. 9, three DC-DC converters are working in parallel and connected to a common DC source bus fed by a 48V DC source. The load bus is regulated at 24 V DC. The loads are comprised of three identical 50Ω resistors connected in parallel. The second and third resistive loads are connected through MOSFET switches at 20 and 40 seconds during the test, respectively. Since each resistor is 50Ω, the simulation starts with 50Ω, and during the test, the total impedance of the load will reduce down to 25Ω and approximately 16Ω after connecting the second and third resistors.

In the case of a power shortage, a Lithium-Ion battery is connected through a bi-directional DC-DC converter to support the grid. The battery voltage level is set to 12V and it will discharge through the boost side of the bi-directional converter to level the battery output voltage up to 24V for supplying the loads. For charging, however, the battery will be energized through the buck side of the bi-directional converter. To do this, the 24V at the load bus is reduced to 12V by a bi-directional DC-DC converter to charge the battery. Fig. 10 illustrates the DT model of the MG in the Typhoon HIL environment.

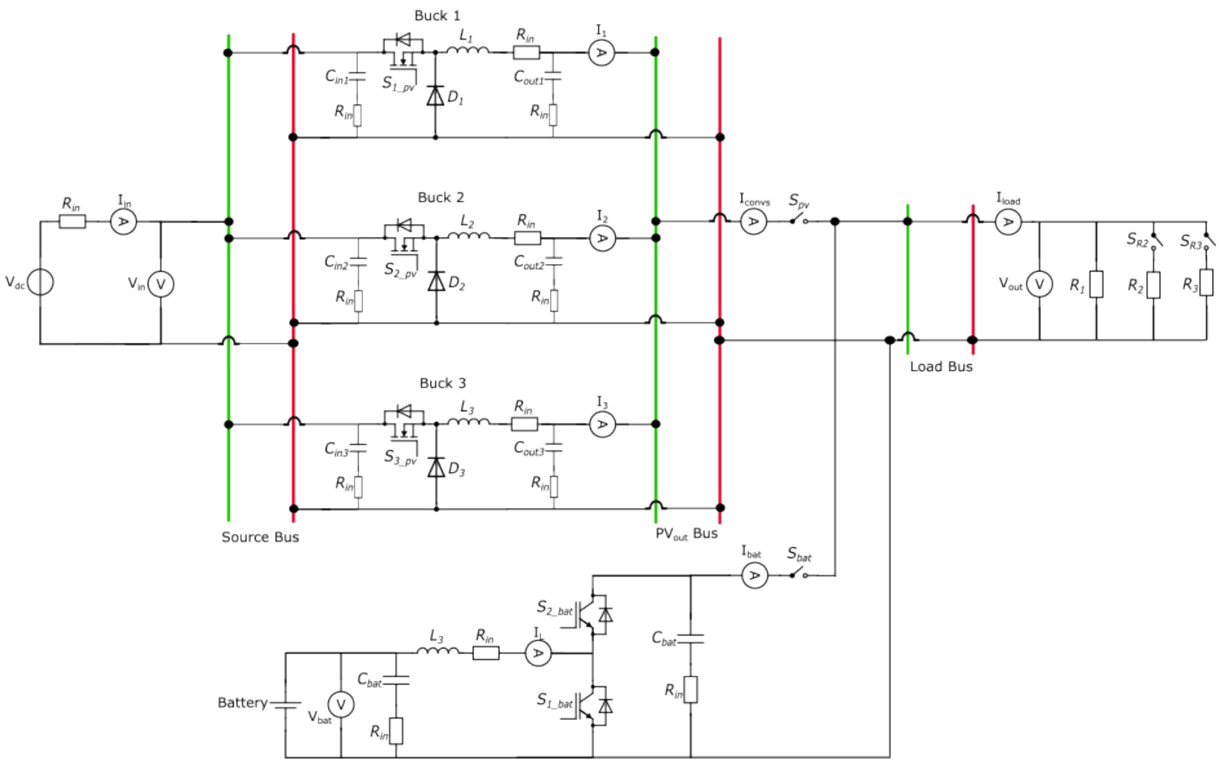

Figure 10: The DT Model in Typhoon HIL Environment

3.2 The MG Physical System (PS)

There are three DC-DC converters working in parallel fed by one DC source providing 48V DC to the common DC source bus. Their outputs supply constant 24V DC for the common load bus connected to three resistive loads. Fig. 11 illustrates an overview of the PS Model of the MG developed by the CARE team at the University of Louisiana at Lafayette.

For the actual system, IT-M3900C Bidirectional Programmable DC Power Supply is used as a main source since it has the capability of solar emulation. Three SPM-FB-KIT converters with the range of 600V | 2.4kW are utilized to supply the load. Since all three converters have the same ratings, converters contribute equally. Table 1 shows rated configurations of different components implemented in the actual MG system.

4. Tests and Results

The performance of the actual system and its DT model is evaluated in two phases. Phase I aims to ensure the DT model is a high-fidelity virtual replica of the system. Since the DT model is comprised of two components including PV and battery systems, Fig. 10, each component's behavior should be evaluated and compared to its actual part for a

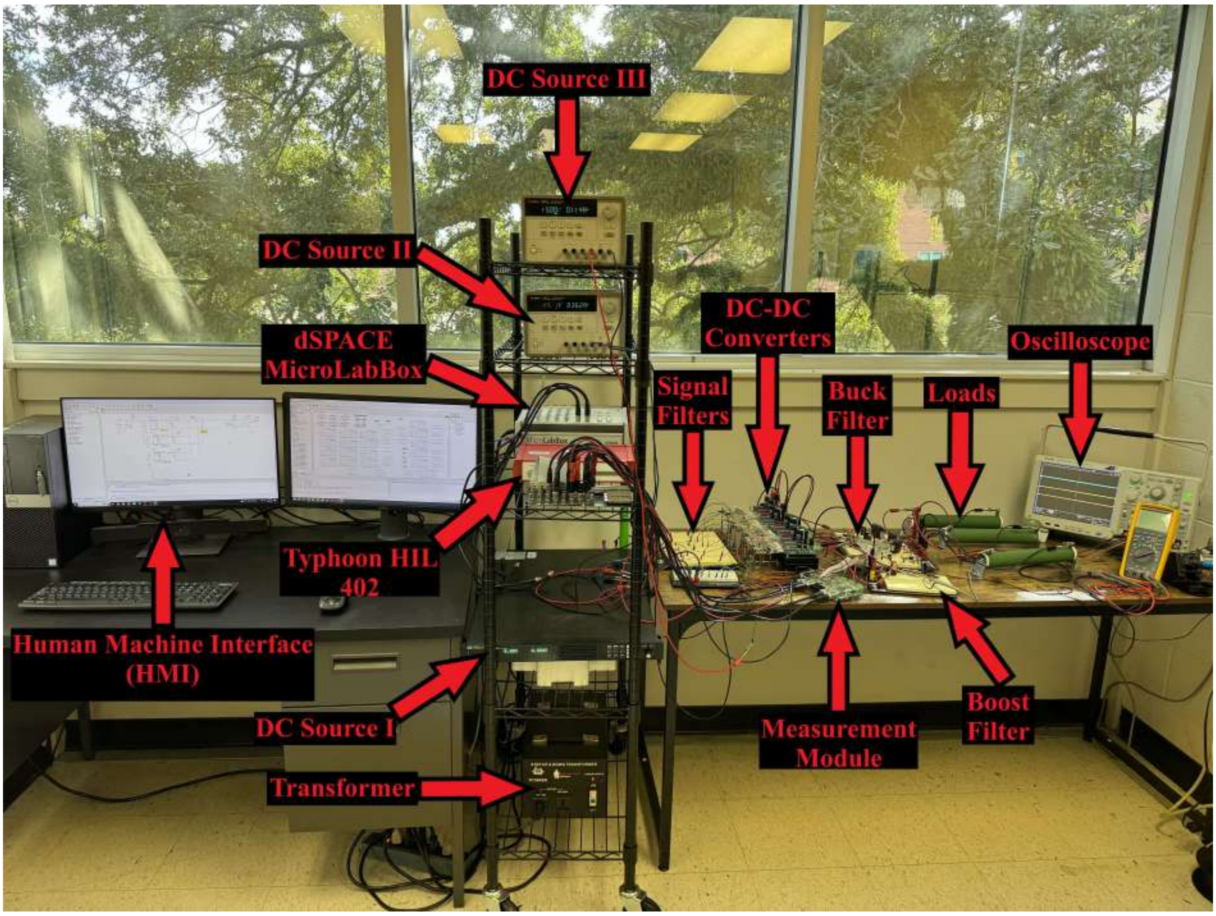

Figure 11: The Actual System at the University of Louisiana at Lafayette

Table 1: Configuration of the actual microgrid system

Position	Component	Parameter	Value	Unit
6*Source	3*DC Source I	Power	+/-12	kW
		Voltage	10-1500	V
		Current	-720 1020	A
	3*DC Sources II, III	Power	25	W
		Voltage	25	V
		Current	1	A
5*Converter	3*Converters I, II, III, IV	Power	2.4	kW
		Voltage	600	V
		Switching Frequency	50	kHZ
	2*Input Capacitor	C	2*480	μF
		$R_{C,in}$	0.1	Ω
8*Filter	4*buck	L	9	mH
		$R_{L,in}$	0.1	Ω
		C	1100	μF
		$R_{C,in}$	0.1	Ω
	4*boost	L	15	mH
		$R_{L,in}$	0.1	Ω
		C	2200	μF
		$R_{C,in}$	0.1	Ω
5*Load	3*Resistive Load	R_1	50	Ω
		R_2	50	Ω
		R_3	50	Ω
	2*MOSFET	Voltage	50	V
		Current	5	A

more accurate fidelity check. Moreover, having a validated DT model can substantially help with critical decision-making in the face of any unforeseen conditions especially if the physical system is on the Moon which is far away from its main control center on Earth. Once the fidelity of the DT model is verified, the DT model can be used instead of the actual system to apply different tests in a safer environment. Thus, the goal of phase II is to test different features of the physical system and its control system under 2 scenarios.

4.1 Phase I - Assessment Tests

To achieve the goal of phase I, the fidelity of the DT model is evaluated under two assessment tests including normal and emergency operations. In the first assessment test, the performance of both DT and PS is evaluated under normal operation (Mode 0). The second assessment test evaluates the performance of the DT and PS under the emergency operation (Mode 3). The simulation starts with one 50Ω resistive load and then the second and third loads are added to the system after 20 and 40 seconds respectively as shown in Fig. 10), respectively.

In addition to the change of load, the DT and PS systems are tested under 3 different voltage configurations. These configurations vary for assessment test I and test II since their circuit models are different. The reason behind this test is to evaluate and compare the performance of the controller under different operating points. As mentioned previously, the main gap in the DT area is how to evaluate the fidelity of a DT model. Thus, the assessment of the DT model in this study is not limited to only change of load.

4.1.1 Assessment Test I - Normal Operation

The first assessment test evaluates the performance of the DT and PS under normal operation. Both DT and PS are evaluated under three voltage configurations including 10-5 V, 24-12 V, and 48-24 V. In these voltage configurations, the first number represents the value of the generation bus and the second one is the rated voltage at the load bus.

Fig. 12 depicts collected real-time data of PS and DT output voltages in 48-24 V configuration from the human-machine interface (HMI). According to the Fig. 12, the DT output voltage follows closely the pattern of the PS. It is worth mentioning that the current sharing is performed using averaging-based distributed control. At t =20 Sec and t=40 Sec, the second and third loads are connected in parallel to the first load. The calculated RMSE and MAPE for this test are 2% and 0.2%, respectively which meets the 5% IEEE standard Castellani et al., 2020; S. Liu et al., 2023. Moreover, the captured output voltages from the oscilloscope for DT and PS are shown in Fig. 13.

Distributed currents in DT and PS as well as the total demand are all shown in Fig. 14. Once the second and third resistive loads are connected, the demand current at the load bus goes up. Therefore, the total current provided increases to approximately 1 A and 1.5 A after the second and third loads are connected.

The currents for each buck agent are illustrated in Fig. 15, Fig. 16, and Fig. 17. According to the figures, the DT model follows closely the physical testbed.

As discussed earlier, the evaluation test is conducted under two other operation points including 10-5 V and 24-12 V. Table 2 shows the RMSE and MAPE calculated for all

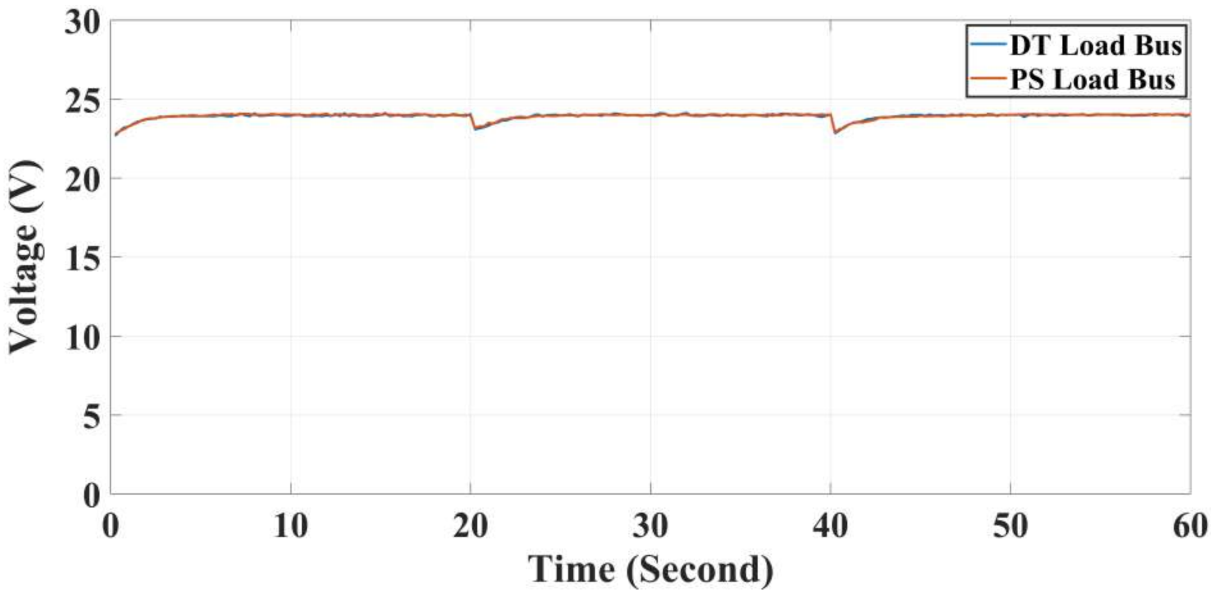

Figure 12: DT model and PS voltage comparison from the HMI in assessment test I

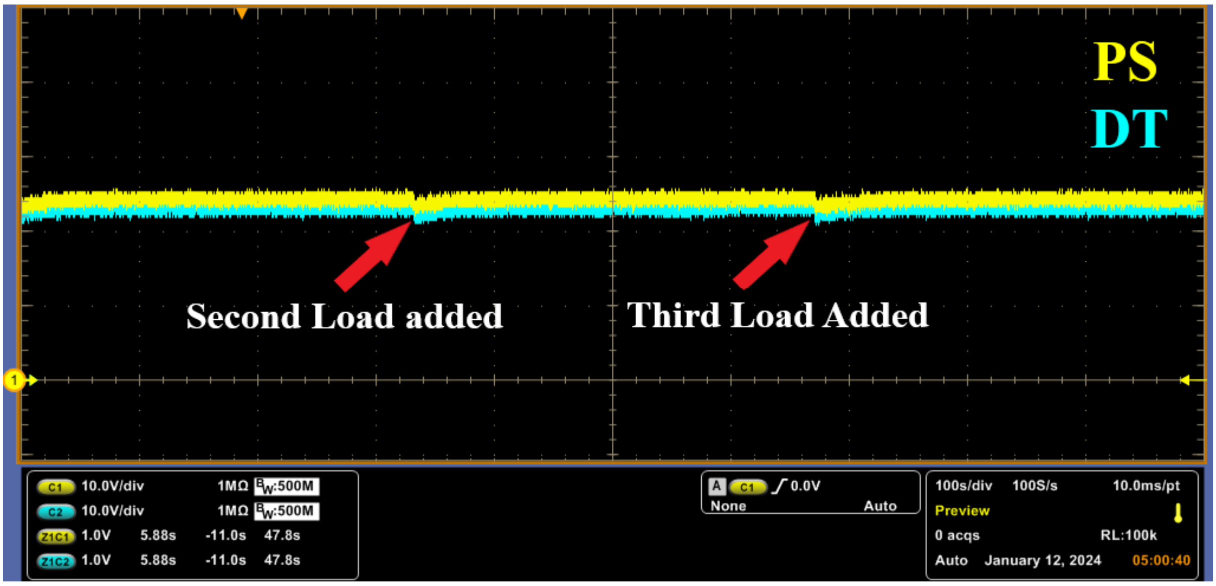

Figure 13: DT model and PS voltage comparison from the oscilloscope in assessment test I

voltage configurations during the assessment test I. According to Table 2, all calculated RMSE and MAPE for the entire assessment test I are equal to or less than 5% meeting IEEE standards Castellani et al., 2020; S. Liu et al., 2023.

Table 2: RMSE and MAPE calculation in assessment test I

Voltage Config. (V)		**2*RMSE (%)**	**2*MAPE (%)**
Source Bus	Load Bus		
10	**5**	2.1	0.2
24	**12**	3.4	0.2
48	**24**	2.3	0.2

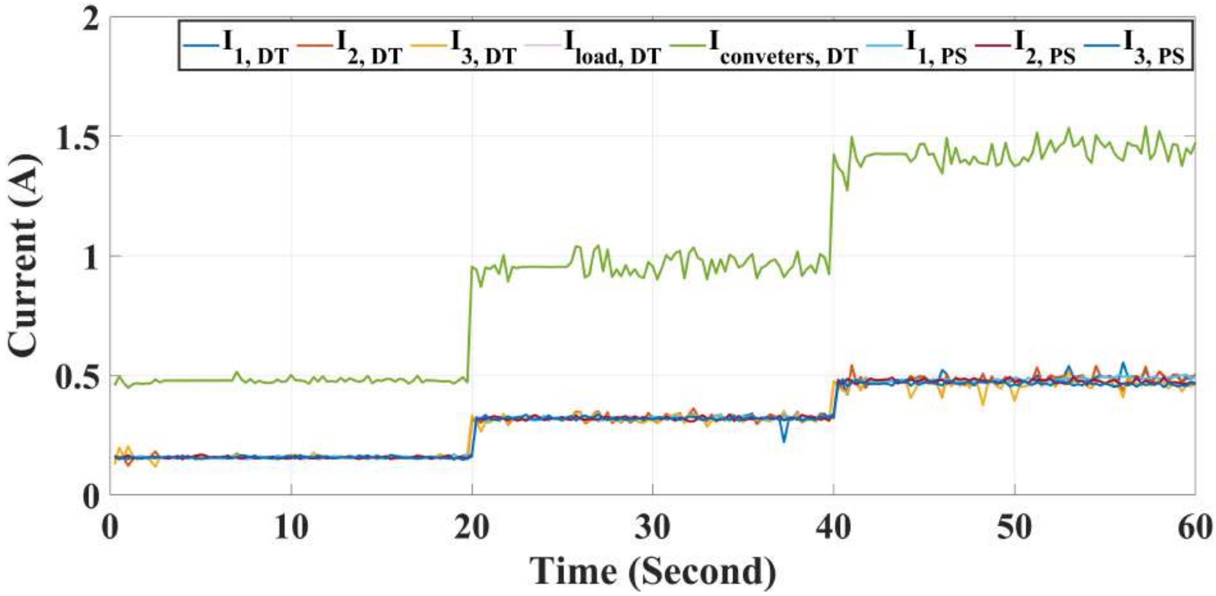

Figure 14: DT model and PS all currents comparison in assessment test I

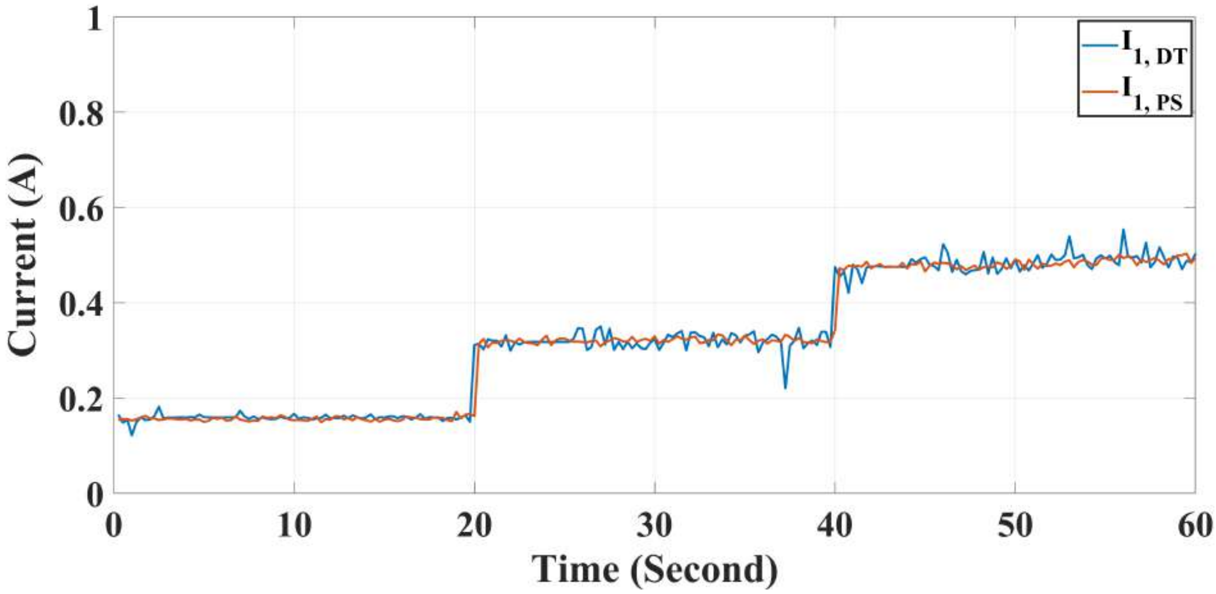

Figure 15: DT model and PS agent buck 1 current comparison in assessment test I

4.1.2 Assessment Test II - Emergency Operation

The second assessment test evaluates the performance of the DT and PS under emergency operation where a battery storage system supports the microgrid under a power shortage and voltage drop scenario.The battery system includes a boost converter controlled with the MPC method. The battery is expected to respond quickly to unexpected conditions where the PV system is not able to fully meet the load demand.

In the emergency operation test, the PV system is disconnected from the DC bus and the controller provides the load in the islanding mode. Unlike the assessment test I, the battery starts serving the $R_1 = 50\ \Omega$ load at the beginning. Then, $R_2 = 50\ \Omega$ and $R_3 = 50\ \Omega$ loads are added in parallel at t=20 Sec and t=40 Sec, respectively. The

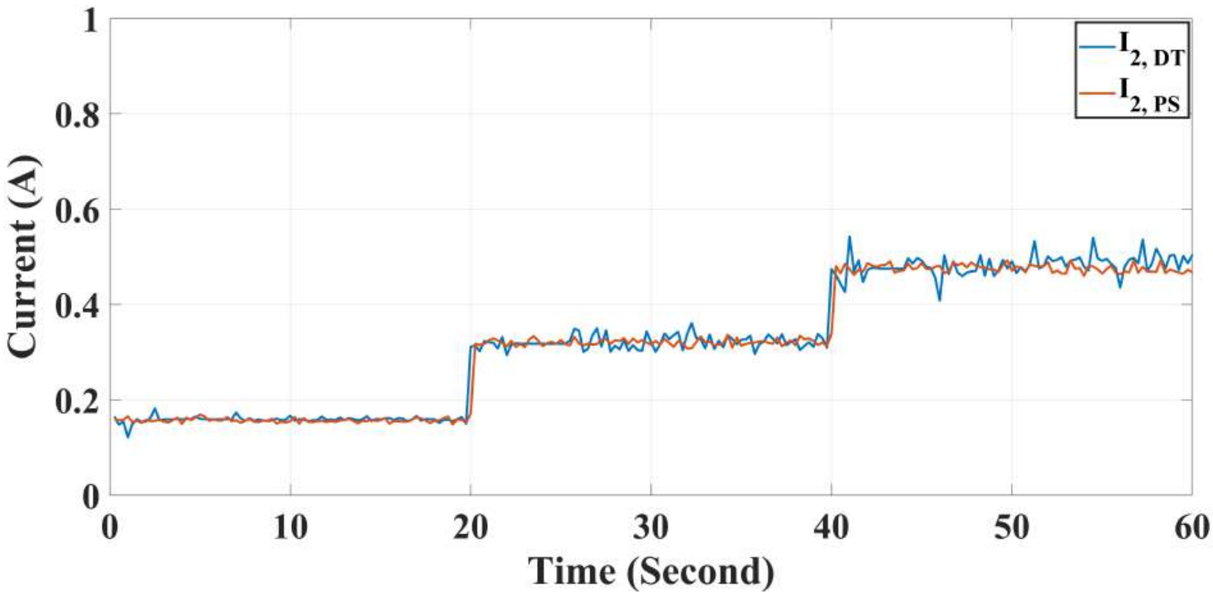

Figure 16: DT model and PS agent buck 2 current comparison in assessment test I

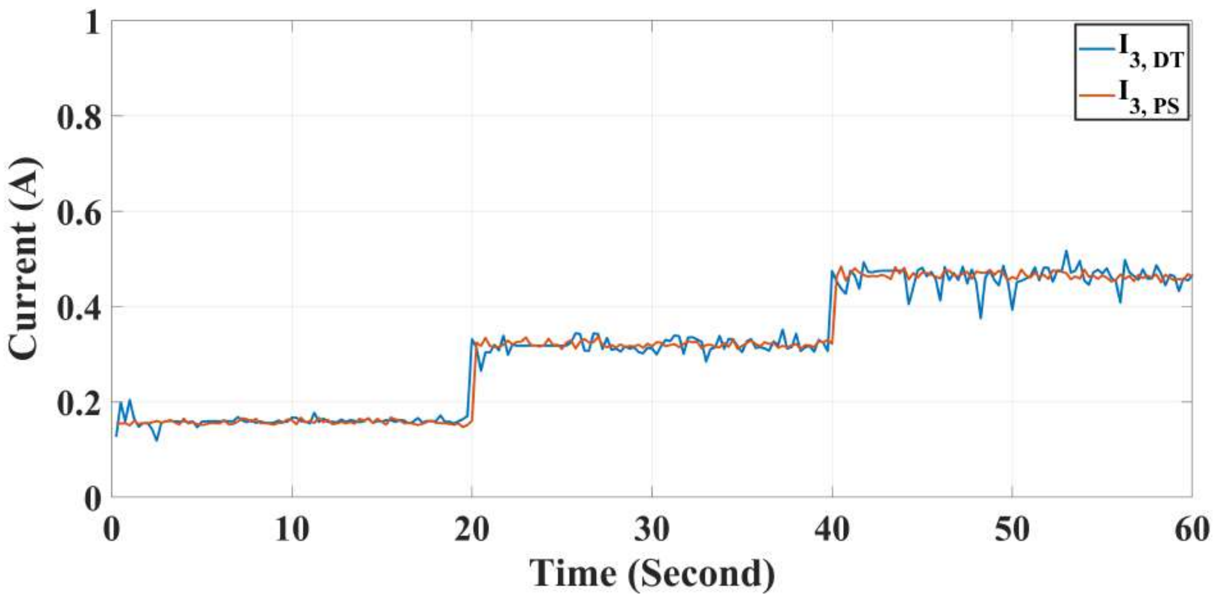

Figure 17: DT model and PS agent buck 3 current comparison in assessment test I

DT and PS performances are assessed under three voltage configurations of 4-8 V, 8-16 V, and 12-24 V. Same as assessment test I, the first number represents the value of the DC source bus and the second one is the value of the DC load bus increased by one DC-DC boost converters. The rated voltage for each battery cell is 4V in our real-time testing environment. Thus, it enables system's operator to connect the required number of battery cells according to the load demand. This reflects an advantage of using DT for running what-if scenarios before making a decision in the physical plant.

Fig. 18 illustrates collected real-time voltage data coming from PS and DT systems in 12-24 V configuration. As can be seen, the DT output voltage chases nearly the pattern of the PS. At t=20 Sec and t=40 Sec, the second and third loads are connected in parallel to the first load. The calculated RMSE and MAPE for this test are 4% and

0.2%, respectively meeting the IEEE standards Castellani et al., 2020; S. Liu et al., 2023. Furthermore, the captured output voltages from the oscilloscope for DT and PS in the test assessment II are illustrated in 19.

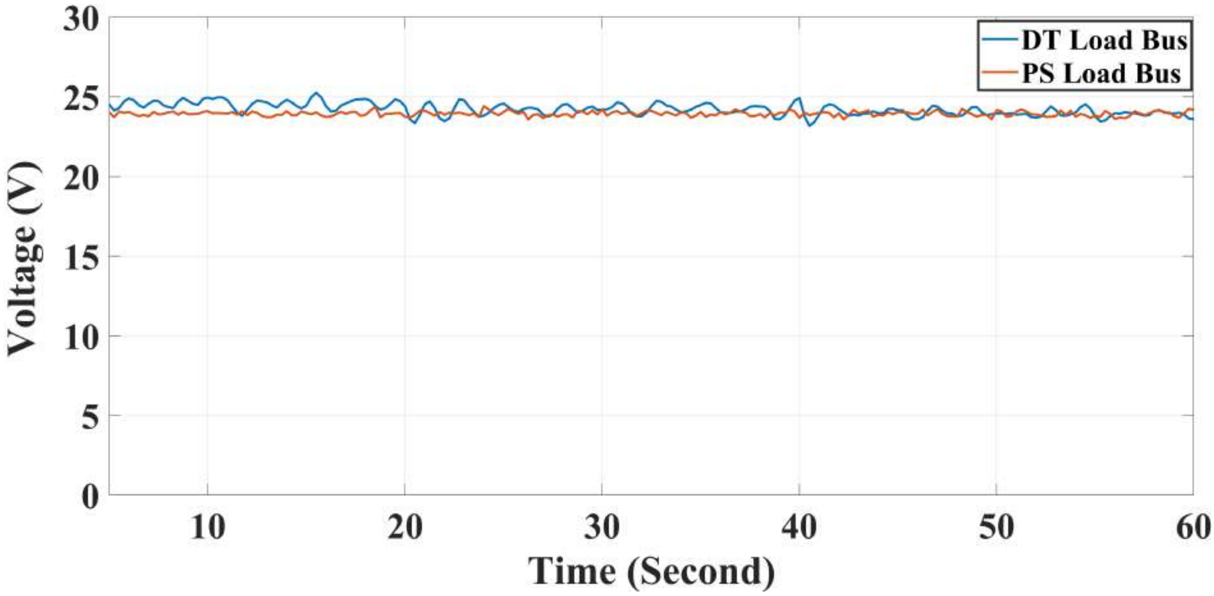

Figure 18: DT model and PS voltage comparison from HMI in assessment test II

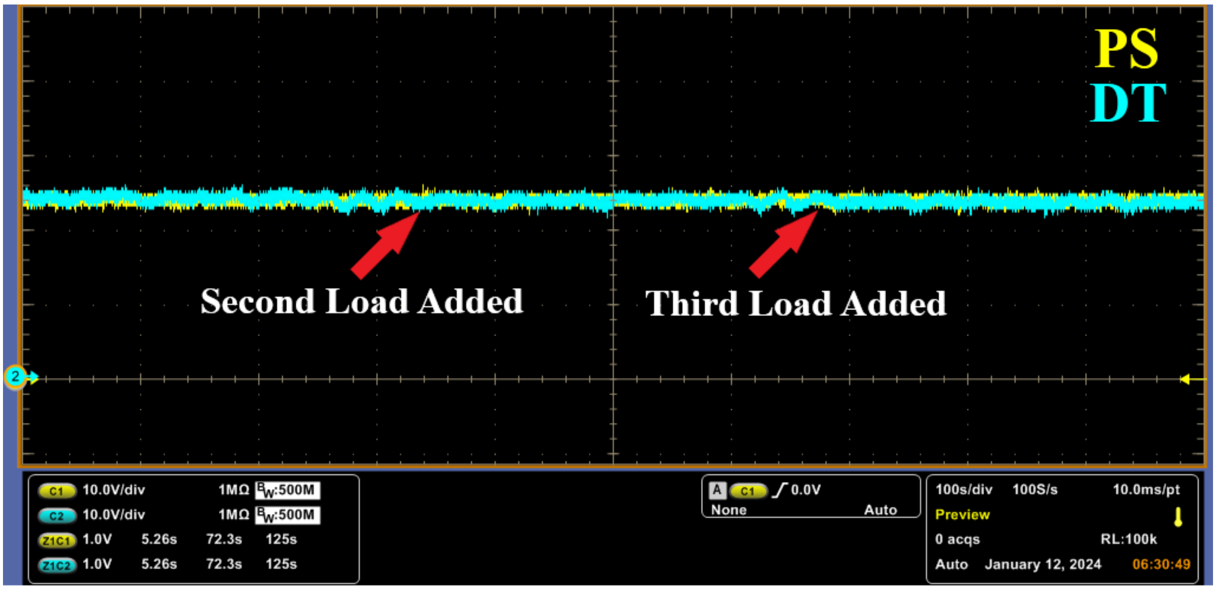

Figure 19: DT model and PS voltage comparison from the oscilloscope in assessment test II

The currents from the DT model and PS are all illustrated in Fig. 20. The figure shows how the controllers respond to the change of load and also how DT follows the testbed in real-time.

The SOC of the battery during the discharging mode can be seen in Fig. 21. Due to the increase in the discharging current, the SOC of the battery decreases faster. According to the figure, the slope of battery SOC is sharpened once the second load is added at t=20 Sec. The same story is true once the third load is connected at t=40 Sec.

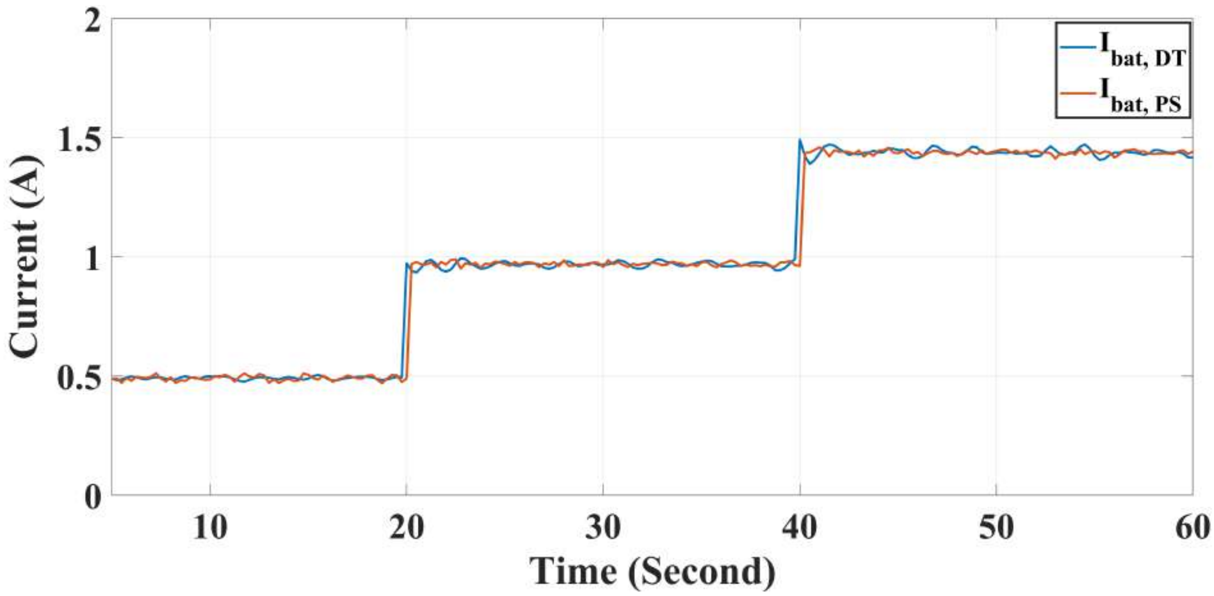

Figure 20: DT model and PS current comparison in assessment test II

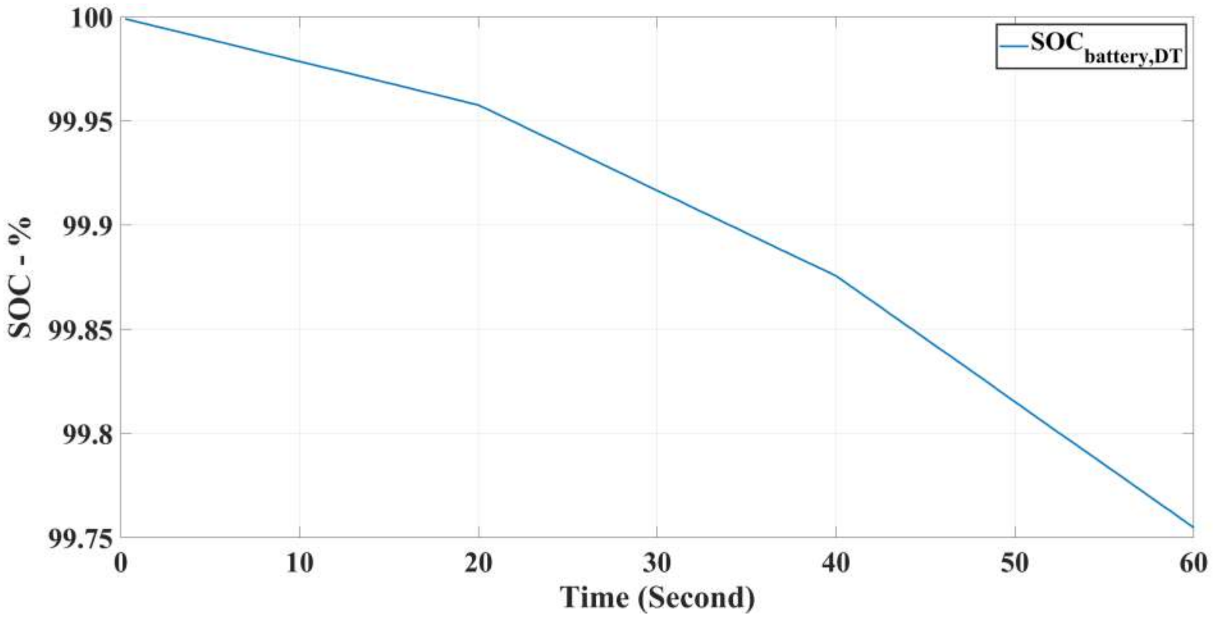

Figure 21: The battery SOC during discharging in assessment test II

To better evaluate the DT model, three different voltage configurations are tested to check the fidelity of the DT model with respect to the PS. The voltage configurations are 4-8 V and 8-16 V. Table 3 presents the RMSE and MAPE calculated for all voltage configurations during the assessment test II.

4.2 Phase II - Performance Tests

Once the fidelity of the DT model is verified, the DT can be used instead of the PS to apply emergency tests since the DT mimics the similar behavior of the PS. In addition, analyzing the outcomes of what-if scenario tests can help identify areas that may need improvements. Therefore, by creating solid plans for each outcome, the PS can be better

Table 3: RMSE and MAPE calculation in assessment test II

Voltage Config. (V)		2*RMSE (%)	2*MAPE (%)
Source Bus	Load Bus		
4	**8**	4.7	0.5
8	**16**	5.1	0.5
12	**24**	5.4	0.5

prepared to handle certain unexpected situations that may arise in the future. Thus, the DT has a vital role to play in enhancing the operation of the PS model, especially in applications where the PS is far away from the control center like a Lunar power system.

To enhance the planning and operation of the PS model, it is essential to apply some tests on the DT model required for emergency response. Therefore, the goal of phase II is to analyze and assess the performance of the PS using its DT model instead, under 2 scenarios to mitigate the effect of any unforeseen issues on the PS model happening on the Moon. Scenario I aims to evaluate the performance of the control unit switching from normal operation mode to islanding mode due to the incapability of solar PV to meet the load demand (Modes 0 & 3).

The battery system must be always ready to support the PV system during power shortage scenarios (e.g., dust impact on the Lunar surface). Thus, scenario II tests the battery charging system which starts working once the PV system has enough power to serve loads. A collaborative battery control is designed where a current sharing and an MPC-based controller are involved. The battery starts charging with the CC mode. After the SOC of the battery reaches a predefined value, the charging mode is switched to the CV. Once the SOC reaches 100 %, the system continues working under normal operation.

4.2.1 Scenario I - Emergency Support Discharging

The first scenario evaluates the performance of the DT under unforeseen emergency conditions. In this scenario, the solar PV system starts serving the loads. Due to a disturbance, it is assumed that the solar power is no longer able to meet the load. At this moment, the battery controller enables the battery discharge mode. The reason for the PV system's power shortage can be either dust on solar panels due to the dusty atmosphere on the Moon or any unexpected issues during the operation.

Fig. 22 illustrates voltages at the solar, battery and load side. According to the figure, after roughly 60 seconds while all loads are connected, the voltage of the PV system suddenly drops. Thus, the MPS-based battery controller, promptly disconnects the PV system from the DC load bus and enables the battery's discharge mode to keep the voltage at the load bus regulated.

The currents for the PV , load, and battery are shown in Fig. 23. From t=0 to t=60 Sec, the PV supplies all the demand. In this scenario, however, the power of the PV system

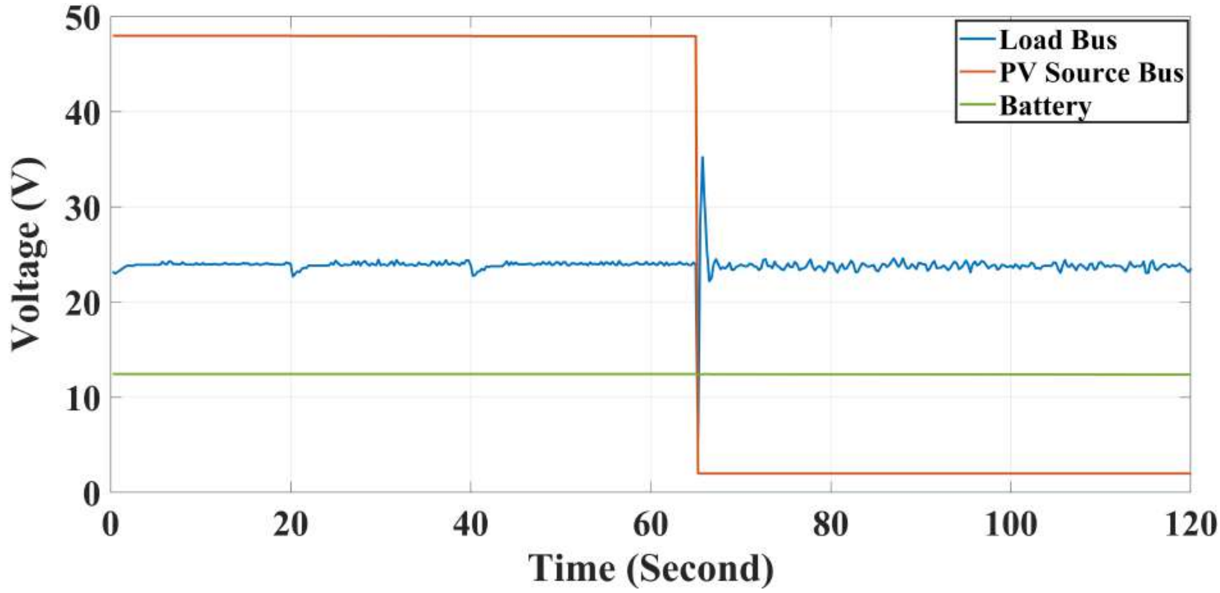

Figure 22: Voltage waveforms in emergency support discharging scenario I

is dropped due to unforeseen issues. Then, the PV system is immediately disconnected from the DC load bus and the battery is connected to meet the load demand. Thus, the current of the battery system jumps from zero to roughly 1.5 A to serve the loads.

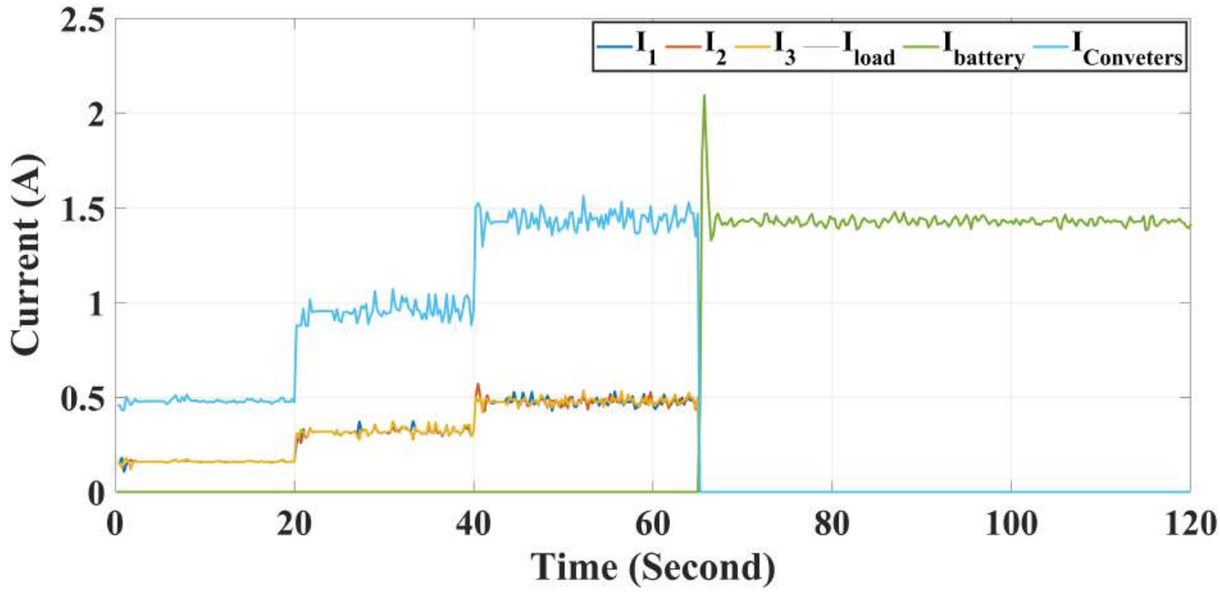

Figure 23: Current waveform in emergency support discharging scenario I

Fig. 24 depicts the SOC of the battery during scenario I, the emergency support test. As shown, the SOC stays at (100 %) while the PV system is serving the loads. After approximately 60 seconds, the battery starts discharging to meet the load demand. Therefore, the SOC of the battery decreases since the battery is discharging.

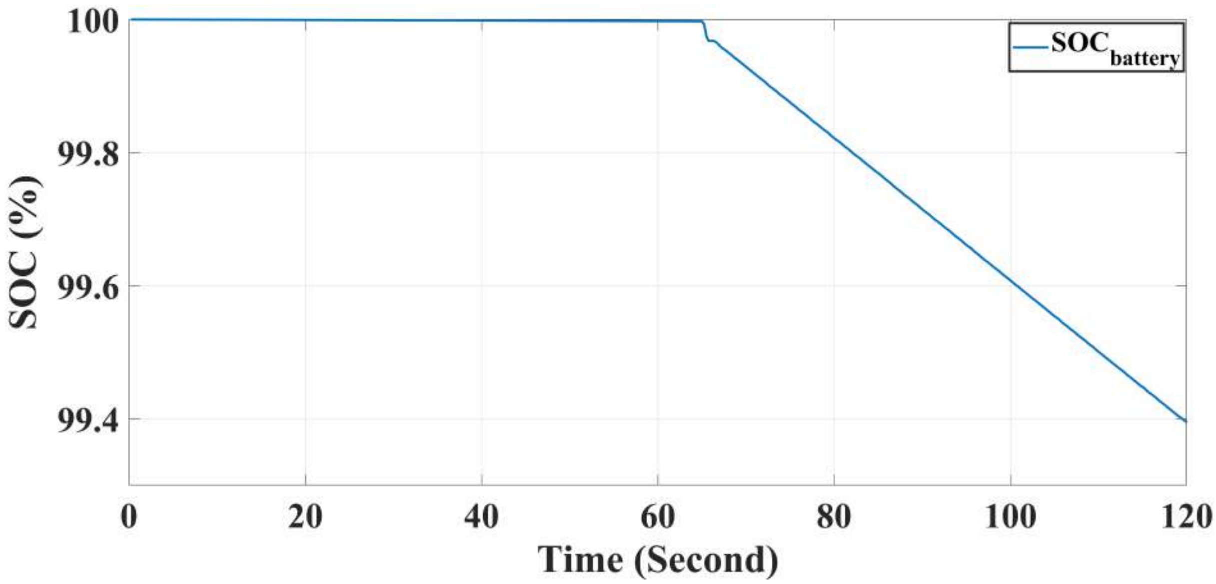

Figure 24: Battery SOC in emergency support discharging scenario I

4.2.2 Scenario II - Emergency Support Charging

The battery modules are expected to be stood by for emergency situations. Therefore, scenario II evaluates the battery charging mechanism, which is activated when the PV system generates sufficient power to support loads and there is a certain amount of excess power. If the SOC of the battery is under a predefined value which in this test is set to 78 %, the battery goes to the CC-based charging mode. In case the SOC is equal to or greater than 78 %, the battery is charged under CV charging mode until the SOC reaches 100%. After that, the battery system is disconnected from the MG, and the solar PV system will fully supply the load in normal operation (mode 0).

Fig. 25 shows the voltages at the solar, battery, and load side. As can be seen, the battery starts charging under CC mode controlled by MPC for approximately five minutes. Once the battery SOC reaches 78%, the charging mode is moved from CC to CV. The battery stays in the charging mode under the CV mode until the SOC reaches 100% (after about 8 minutes and 20 seconds). Eventually, the battery is disconnected and the PV stays as the only source serving the loads. During all charging modes and switching back to normal operation, the voltage of the load bus remains steady at 24 V. This is because of a collaboration between the current sharing technique and the MPC control on the battery side.

The currents at the load side as well as battery and solar PV are all shown in Fig. 26. Since the SOC of the battery is less than 78%, the battery control starts with the CC mode. In this mode the battery is charged with a constant current of 1 A. This charging current is provided by three DC-DC buck converters connected to the PV system. Since the three buck converters are identical, each buck agent, therefore, is responsible for one-third of the charging current as well as one-third of the loads demanded current.

Once the SOC reaches 78%, the charging mode is changed to CV. In this charging

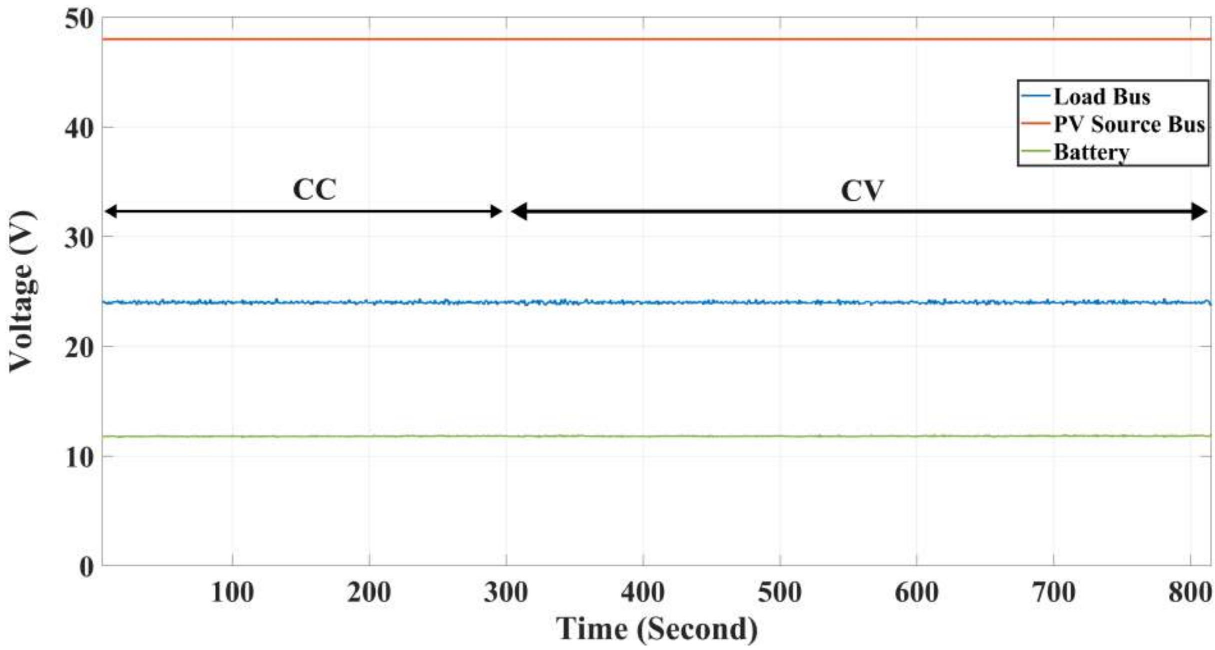

Figure 25: Voltage waveforms in emergency support charging scenario II

mode, the MPC regulates the battery's voltage at 12 V. As the SOC goes up, the charging current decreases. Therefore, the currents provided by the buck converters reduce as well. After the battery is fully charged, the battery is immediately disconnected from the DC load bus and the PV system continues serving the loads. It is worth noting that during both CC and CV charging modes, the loads keep receiving a constant current of approximately 1.5 A which shows a good collaboration between the current sharing technique and the battery MPC controller.

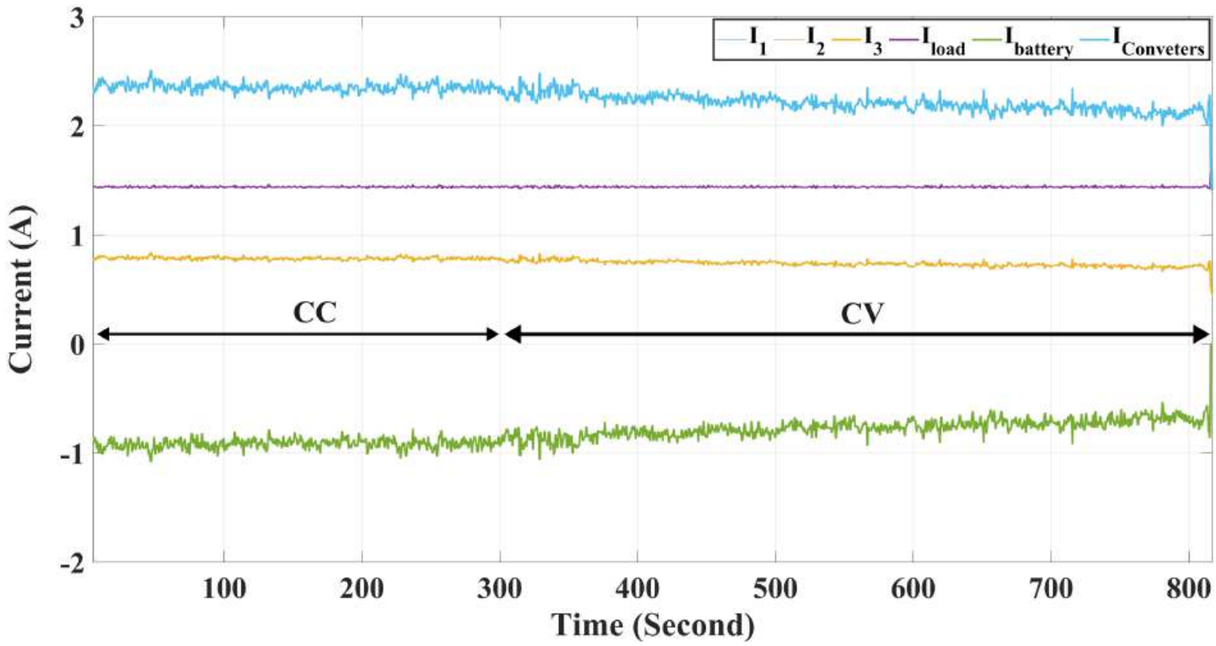

Figure 26: Current waveform in emergency support charging scenario II

Fig. 27 depicts the SOC of the battery during the scenario II emergency support charging test. According to the figure, the SOC is 60% at the beginning of the test. Thus, the MPC starts charging the battery under the CC mode for about five minutes. Once the SOC reaches the predefined value (78%), the battery goes to the CV charging mode. This charging mode takes approximately 500 seconds until the battery is fully charged.

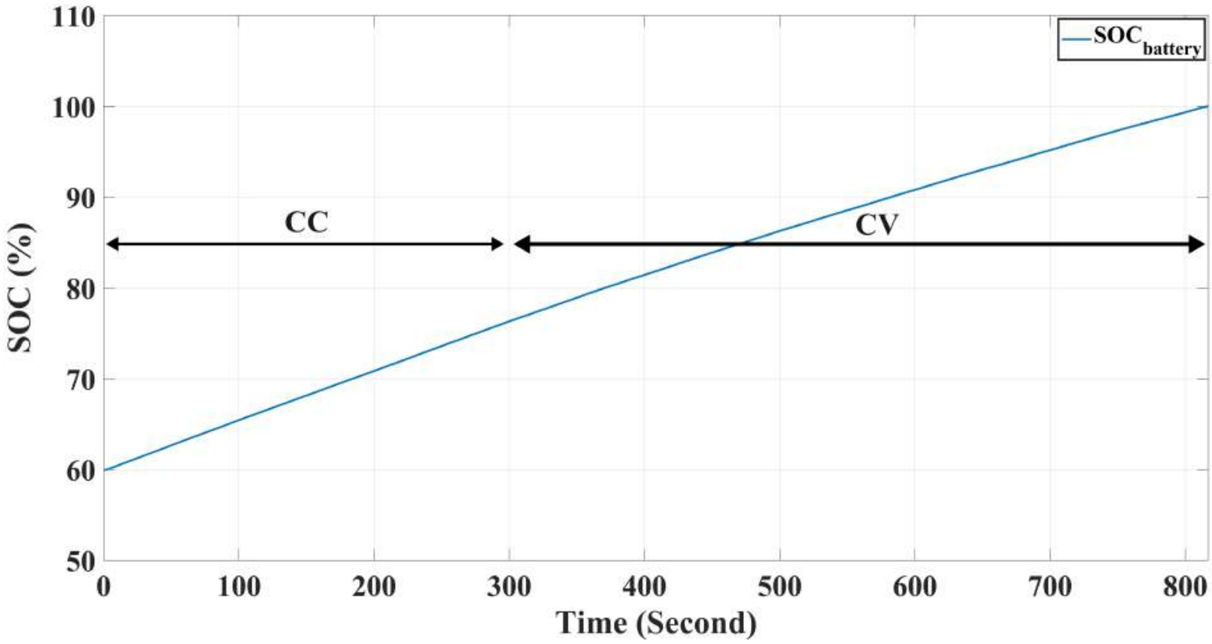

Figure 27: Battery SOC in emergency support charging scenario II

5. Conclusion

Utilizing digital twin technology for a nanogrid plant, our system demonstrates high-fidelity real-time representation with low root mean square error values. The digital twin's innovation lies in its ability to simulate scenarios beyond existing controllers, fortifying system resilience against unforeseen events. This approach, particularly valuable where physical access is limited, empowers operators to proactively respond to disruptions. The integration of a modular battery storage solution enhances the system's capability to address challenges such as the dust effect on the Lunar surface or unexpected faults. Overall, our holistic approach not only validates space-based power system resilience but also lays the foundation for transformative advancements in handling uncertainties during space missions.

6. Acknowledgement

Authors would like to express their gratitude to NASA's Stennis Space Center (SSC) and Glenn Research Center (GRC) for valuable insights and feedback during several technical meetings.

References

Allen, B. D. (2021). Digital twins and living models at nasa. *Digital Twin Summit*.

Artemis. (2022). *Humanity's return to the moon*. https://www.nasa.gov/feature/artemis/ (accessed: October 2023).

Bazmohammadi, N., Madary, A., Vasquez, J. C., Mohammadi, H. B., Khan, B., Wu, Y., & Guerrero, J. M. (2022). Microgrid digital twins: Concepts, applications, and future trends. *IEEE Access*, 10, 2284–2302. https://doi.org/10.1109/ACCESS.2021.3138990

Beguery, P., Pflaum, P., & Mugnier, C. (2019). Microgrid energy management optimization - a common platform for research, development and design tools. *Proceedings of Building Simulation 2019: 16th Conference of IBPSA*, 16, 3163–3170. https://doi.org/https://doi.org/10.26868/25222708.2019.210183

Béguery, P., Pflaum, P., & Mugnier, C. (2019). Microgrid energy management optimization-a common platform for research, development and design tools. *Building Simulation 2019*, 16, 3163–3170.

Brenna, M., Foiadelli, F., Leone, C., & Longo, M. (2020). Electric vehicles charging technology review and optimal size estimation. *Journal of Electrical Engineering & Technology*, 15, 2539–2552.

Castellani, A., Schmitt, S., & Squartini, S. (2020). Real-world anomaly detection by using digital twin systems and weakly supervised learning. *IEEE Transactions on Industrial Informatics*, 17(7), 4733–4742.

Cheng, T., Zhu, X., Yang, F., & Wang, W. (2023). Machine learning enabled learning based optimization algorithm in digital twin simulator for management of smart islanded solar-based microgrids. *Solar Energy*, 250, 241–247.

Deren, L., Wenbo, Y., & Zhenfeng, S. (2021). Smart city based on digital twins. *Computational Urban Science*, 1, 1–11.

DoE, U. (2003). Grid 2030: A national vision for electricity's second 100 years. *US DOE Report*, 137–140.

Ebrahimi, S., Safayet Ullah, S., & Ferdowsi, F. (2022). Adaptable low-cost volt-var control for smart pv inverters. *2022 North American Power Symposium (NAPS)*, 1–5. https://doi.org/10.1109/NAPS56150.2022.10012193

Ebrahimi, S., Safayet Ullah, S., Yankson, S., & Ferdowsi, F. (2024). Advancing fault detection and classification through high-fidelity digital twin simulation and ai. *2024 IEEE Texas Power and Energy Conference (TPEC)*, 1–5.

Ebrahimi, S., Ullah, S. S., & Ferdowsi, F. (2024). Adaptable volt-var control digital twinning for smart solar inverters. *Renewable Energy Focus*, 48, 100525.

Ebrahimi, S., Ullah, S. S., Ferdowsi, F., & Barati, M. (2022). Machine learning-aided anomaly detection for secure smartification of solar inverters. *2022 IEEE Kan-*

sas Power and Energy Conference (KPEC), 1–6. https://doi.org/10.1109/KPEC54747.2022.9814799

Eirinakis, P., Kalaboukas, K., Lounis, S., Mourtos, I., Rožanec, J. M., Stojanovic, N., & Zois, G. (2020). Enhancing cognition for digital twins. *2020 IEEE International Conference on Engineering, Technology and Innovation (ICE/ITMC)*, 1–7.

Garfinkel, J. (2018). Gartner identifies the top 10 strategic technology trends for 2019. *by Gartner. URL: https://www. gartner. com/en/newsroom/pressreleases/2018-10-15-gartner-identifies-the-top-10-strategictechnology-trends-for-2019 (visited on 09/11/2019)*.

Ghanbari, N., & Bhattacharya, S. (2020). Adaptive droop control method for suppressing circulating currents in dc microgrids. *IEEE Open Access Journal of Power and Energy*, 7, 100–110.

Hong, Y.-Y., & Apolinario, G. F. D. (2022). Ancillary services and risk assessment of networked microgrids using digital twin. *IEEE Transactions on Power Systems*.

Laaki, H., Miche, Y., & Tammi, K. (2019). Prototyping a digital twin for real time remote control over mobile networks: Application of remote surgery. *Ieee Access*, 7, 20325–20336.

Li, Q., Cui, Z., Cai, Y., & Su, Y. (2023). Multi-objective operation of solar-based microgrids incorporating artificial neural network and grey wolf optimizer in digital twin. *Solar Energy*, 262, 111873.

Li, Q., Cui, Z., Cai, Y., Su, Y., & Wang, B. (2023). Renewable-based microgrids' energy management using smart deep learning techniques: Realistic digital twin case. *Solar Energy*, 250, 128–138.

Liu, S., Bao, J., & Zheng, P. (2023). A review of digital twin-driven machining: From digitization to intellectualization. *Journal of Manufacturing Systems*, 67, 361–378.

Liu, Y., Zhang, L., Yang, Y., Zhou, L., Ren, L., Wang, F., Liu, R., Pang, Z., & Deen, M. J. (2019). A novel cloud-based framework for the elderly healthcare services using digital twin. *IEEE access*, 7, 49088–49101.

Lopez, J. R., de Jesus Camacho, J., Ponce, P., MacCleery, B., & Molina, A. (2022). A real-time digital twin and neural net cluster-based framework for faults identification in power converters of microgrids, self organized map neural network. *Energies*, 15(19), 7306.

NASA. (2023). *Weather on the moon*. https://moon.nasa.gov/inside-and-out/dynamic-moon/weather-on-the-moon/ (accessed: October 2023).

Padmawansa, N., Gunawardane, K., Madanian, S., & Than Oo, A. M. (2023). Battery energy storage capacity estimation for microgrids using digital twin concept. *Energies*, 16(12), 4540.

Pan, H., Dou, Z., Cai, Y., Li, W., Lei, X., & Han, D. (2020). Digital twin and its application in power system. *2020 5th International Conference on Power and Renewable Energy (ICPRE)*, 21–26.

Pan, M., Xing, Q., Chai, Z., Zhao, H., Sun, Q., & Duan, D. (2023). Real-time digital twin machine learning-based cost minimization model for renewable-based microgrids considering uncertainty. *Solar Energy*, 250, 355–367.

Pileggi, P., Verriet, J., Broekhuijsen, J., van Leeuwen, C., Wijbrandi, W., & Konsman, M. (2019). A digital twin for cyber-physical energy systems. *2019 7th Workshop on Modeling and Simulation of Cyber-Physical Energy Systems (MSCPES)*, 1–6. https://doi.org/10.1109/MSCPES.2019.8738792

Qi, Q., & Tao, F. (2018). Digital twin and big data towards smart manufacturing and industry 4.0: 360 degree comparison. *Ieee Access*, 6, 3585–3593.

Rajesh, J., Nisha, K., Bonala, A. K., & Sandepudi, S. R. (2019). Predictive control of three level boost converter interfaced spv system for bi-polar dc micro grid. *2019 IEEE International Conference on Electrical, Computer and Communication Technologies (ICECCT)*, 1–6.

Rivera, M., Rodriguez, J., & Vazquez, S. (2016). Predictive control in power converters and electrical drives—part i. *IEEE Transactions on Industrial Electronics*, 63(6), 3834–3836.

Saad, A., Faddel, S., & Mohammed, O. (2020). Iot-based digital twin for energy cyber-physical systems: Design and implementation. *Energies*, 13(18), 4762.

Shafto, M., Conroy, M., Doyle, R., Glaessgen, E., Kemp, C., LeMoigne, J., & Wang, L. (2012). Nasa technology roadmap: Modeling, simulation. *Information Technology & Processing Roadmap Technology Area*, 11.

Toth, R., Heuberger, P. S., & Van den Hof, P. M. (2010). Discretisation of linear parameter-varying state-space representations. *IET control theory & applications*, 4(10), 2082–2096.

Yang, X., Ran, Y., Zhang, G., Wang, H., Mu, Z., & Zhi, S. (2022). A digital twin-driven hybrid approach for the prediction of performance degradation in transmission unit of cnc machine tool. *Robotics and Computer-Integrated Manufacturing*, 73, 102230.

Yuan, G., & Xie, F. (2023). Digital twin-based economic assessment of solar energy in smart microgrids using reinforcement learning technique. *Solar Energy*, 250, 398–408.